

A Cautionary Tale of Attenuation in Star Forming Regions

Mallory Molina^{1,2,*}, Nikhil Ajgaonkar³, Renbin Yan³, Robin Ciardullo¹, Caryl Gronwall¹, Michael Eracleous¹, Médéric Boquien⁴ and Donald P. Schneider¹

¹*Department of Astronomy and Astrophysics and Institute for Gravitation and the Cosmos, The Pennsylvania State University 525 Davey Lab, University Park, PA 16802, USA*

²*eXtreme Gravity Institute, Department of Physics, Montana State University, Bozeman, MT 59715, USA*

³*Department of Physics and Astronomy, University of Kentucky, 505 Rose St., Lexington, KY 40506-0057, USA*

⁴*Centro de Astronomía (CITEVA), Universidad de Antofagasta, Avenida Angamos 601, Antofagasta 1270300, Chile*

Accepted XXX. Received YYY; in original form ZZZ

ABSTRACT

The attenuation of light from star forming galaxies is correlated with a multitude of physical parameters including star formation rate, metallicity and total dust content. This variation in attenuation is even more evident on kiloparsec scales, which is the relevant size for many current spectroscopic integral field unit surveys. To understand the cause of this variation, we present and analyse *Swift*/UVOT near-UV (NUV) images and SDSS/MaNGA emission-line maps of 29 nearby ($z < 0.084$) star forming galaxies. We resolve kiloparsec-sized star forming regions within the galaxies and compare their optical nebular attenuation (i.e., the Balmer emission line optical depth, $\tau_B^l \equiv \tau_{H\beta} - \tau_{H\alpha}$) and NUV stellar continuum attenuation (via the NUV power-law index, β) to the attenuation law described by Battisti et al. We show the data agree with that model, albeit with significant scatter. We explore the dependence of the scatter of the β - τ_B^l measurements from the star forming regions on different physical parameters, including distance from the nucleus, star formation rate and total dust content. Finally, we compare the measured τ_B^l and β values for the individual star forming regions with those of the integrated galaxy light. We find a strong variation in β between the kiloparsec scale and the larger galaxy scale that is not seen in τ_B^l . We conclude that the sight-line dependence of UV attenuation and the reddening of β due to the light from older stellar populations could contribute to the scatter in the β - τ_B^l relation.

Key words: dust, extinction – galaxies: general – galaxies: ISM

1 INTRODUCTION

Attenuation relations describe how the light from both the stellar continuum and nebular emission are affected by dust intrinsic to the source. They differ from extinction laws as they account for the dust, gas, and stars commingling within the observed aperture, which is appropriate for most extragalactic observations. Calzetti et al. (1994) found a relation between the difference in attenuation experienced by the stellar continuum and that affecting the nebular emission in the integrated galaxy light from local ultra-violet (UV)-bright starburst galaxies. The relation was quantified by Calzetti et al. (2000) as $E(B-V)_{\text{star}} = 0.44E(B-V)_{\text{gas}}$, which was used to derive attenuation as a function of wavelength in the UV band. In response to this empirical result, Charlot & Fall (2000) described a physical model where the line-

emitting gas is concentrated near star forming regions which are enshrouded in dust, while older stars are more evenly distributed among the diffuse interstellar medium; therefore the observed stellar continuum is not as strongly affected by attenuation as nebular emission. The Calzetti law was updated by Battisti et al. (2016, hereafter B16) for application to the unresolved nuclear regions of local ($z \lesssim 0.1$) Sloan Digital Sky Survey (SDSS) galaxies, and systems with much lower star formation rates (SFRs; $\log[\text{SFR}/(M_{\odot} \text{ yr}^{-1})] < 1.6$).

In general, attenuation laws have three distinct components: the general shape, which approaches a power law in the UV band, the relation between the stellar and nebular attenuation, and the presence of excess attenuation at 2175 Å (commonly referred to as the 2175 Å bump). All three components can individually correlate with the intrinsic properties of the galaxy, which include SFR, mass, optical opacity, and total attenuation (Charlot & Fall 2000; Calzetti et al. 2000; Calzetti 2001; Wild et al. 2011; Xiao

* E-mail: mallory.molina@montana.edu (MM)

et al. 2012; Salim et al. 2018). The assumed attenuation law will strongly impact any estimate of SFRs determined from the UV stellar continuum, which traces recent star formation (Age $\lesssim 100$ –200 Myr, see Kennicutt 1998; Kennicutt & Evans 2012; Calzetti 2013, for a complete review). Adding to that complication, the UV band is where most of the differences in the attenuation laws lie (see Calzetti et al. 2000; Salim et al. 2018, for a review and update). Understanding UV attenuation is especially important at higher redshifts, where the rest-frame UV is often the only accessible band for exploring star formation and other activity in galaxies. Therefore the choice of attenuation law is critical for accurately measuring recent star formation, both in nearby and more distant galaxies.

Unfortunately, the physical properties that correlate with the overall shape of the attenuation law, such as the dust composition and distribution relative to the stars and gas, all change across the face of a galaxy (Charlot & Fall 2000; Calzetti et al. 2000; Wild et al. 2011; Xiao et al. 2012). There is ample evidence of variations in attenuation curves, not only from galaxy to galaxy, but also within galaxies themselves (Buat et al. 2002, 2005; Gordon et al. 2004; Kong et al. 2004; Calzetti et al. 2005; Boissier et al. 2007; Dale et al. 2009; Boquien et al. 2009, 2012; Decleir et al. 2019). With the advent of IFU surveys such as the Spectrographic Area Unit for Research on Optical Nebulae (SAURON; Bacon et al. 2001), ATLAS^{3D} (Cappellari et al. 2011), DiskMass (Bershady et al. 2010), the Calar Alto Legacy Integral Field Area Survey (CALIFA; Sánchez et al. 2012, 2016; Walcher et al. 2014), the Sydney-Australian Astronomical Observatory Multi-Object Integral Field Spectrograph (SAMI; Croom et al. 2012) and the Mapping Nearby Galaxies at Apache Point Observatory (MaNGA; Bundy et al. 2015; Yan et al. 2016; Blanton et al. 2017), we are no longer limited by data, but by our understanding of local attenuation and SFR estimates.

In order to understand the appropriate attenuation law for the spatially resolved emission prevalent in current IFU surveys, we set out to test the validity of the B16 model for *spatially resolved*, kpc-sized star forming regions across the faces of local star forming galaxies. The work of B16 utilized a set of galaxies with lower star formation rates than Calzetti et al. (1994, 2000), and their results are therefore more representative of the average local star forming galaxy population (i.e., the sample from B16 has $-3.66 \leq \log[\text{SFR}/(M_{\odot} \text{ yr}^{-1})] \leq 1.6$, while that of Calzetti et al. (1994, 2000) has $0 \lesssim \log[\text{SFR}/(M_{\odot} \text{ yr}^{-1})] \lesssim 1.7$). We expand on their work by not only exploring spatially-resolved star forming regions across the faces of galaxies, but also by comparing those individual regions to the integrated galaxy light. Therefore this work explores the effects of aperture size on the attenuation of UV stellar continua and optical nebular emission in star forming galaxies. To effectively resolve regions within a galaxy, we combine data from the *Swift* Ultraviolet Optical Telescope (UVOT; Roming et al. 2005) and the SDSS/MaNGA survey (Bundy et al. 2015; Yan et al. 2016). While the *Galaxy Evolution Explorer* (GALEX; Martin et al. 2005) could give us a wider UV spectral range and is often used in attenuation studies, our emphasis on spatial resolution demands better image quality than the 5'' produced by GALEX.

Section 2 introduces the sample. Our goal is to mea-

sure the Balmer decrement and the UV spectral slope in resolved, kpc-sized star forming regions. In Section 3 we discuss the basic data reduction; in Section 4 we list the requirements for a galaxy to be classified as star forming and compare GALEX to UVOT UV slope measurements, and give the criteria for defining star forming regions within the galaxy in Section 5. In Section 6, we compare the results to the attenuation relation for the unresolved nuclear regions of star forming galaxies as described by B16. After assessing the effectiveness of the B16 law for individual regions, we explore the effect of physical properties, such as metallicity and SFR, on the observed scatter between the measurements and the B16 law. In Section 7 we study the dependence of the observed scatter on galaxy properties, and quantify the change in total attenuation for both the UV stellar continuum and the optical nebular emission between the individual, kpc-sized star forming regions and the integrated galaxy light for the star forming galaxies in our sample. We summarize our findings and present our conclusions in Section 8. We assume a Λ CDM cosmology when quoting masses, distances, and luminosities, with $\Omega_m = 0.3$, $\Omega_{\Lambda} = 0.7$ and $H_0 = 70 \text{ km s}^{-1} \text{ Mpc}^{-1}$.

2 THE SAMPLE

This paper explores a subset of a larger sample that was chosen to study star formation and its quenching in the local universe. Our approach is to simultaneously analyse the near-UV (NUV) stellar continuum and optical nebular emission lines across the faces of galaxies, using data that are well matched in depth and physical scale. While this paper focuses on star forming galaxies as defined in Section 4, we present the basic properties of the total sample, including criteria for selection and basic data reduction.

2.1 SDSS-IV/MaNGA and *Swift*/UVOT

Our sample is drawn from the larger MaNGA survey (Bundy et al. 2015; Yan et al. 2016), which is one of the three major surveys in the fourth generation of SDSS (SDSS-IV; Blanton et al. 2017). Target selection for the MaNGA survey is built on four basic requirements: (1) a sample size of $\sim 10,000$ galaxies, (2) a uniform distribution in stellar mass above $M_* > 10^9 M_{\odot}$, as approximated by the SDSS *i*-band absolute magnitude, (3) uniform spatial coverage in units of half-light radius, and (4) maximized signal-to-noise ratio and spatial resolution (Wake et al. 2017). The MaNGA data were taken with hexagonal IFU fiber bundles that are mounted on the Sloan 2.5-m telescope (Gunn et al. 2006), observing up to 17 objects simultaneously. The IFU bundles can contain anywhere from 19 to 127 2'' fibers, and feed into the dual-channel Baryon Oscillation Spectroscopic Survey (BOSS) spectrographs (Smei et al. 2013; Drory et al. 2015). The resulting spectra cover the wavelength range of 3,622–10,354 Å at a resolving power of $R \sim 2000$. The telescope is dithered to achieve near-critical sampling of the point-spread function (PSF), which has a full width at half maximum FWHM $\approx 2''.5$. Meanwhile the data cubes have a spatial sampling of $0''.5$. These spectra provide the necessary coverage for the use of most nebular diagnostics, including

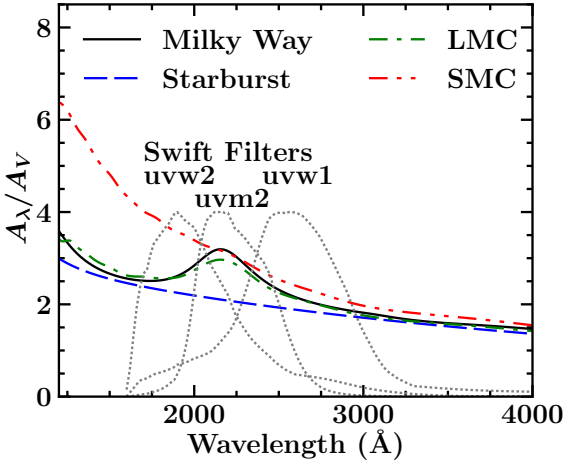


Figure 1. The *Swift*/UVOT uvw2, uvm2 and uvw1 NUV filter relative transmission curves (gray dotted lines) overlaid on the Cardelli et al. (1989) Milky Way extinction curve shown in a black solid line, the Large and Small Magellanic Cloud extinction curves from Gordon et al. (2003) in the green dash-dot line and red dash-dot-dot lines respectively, and the Calzetti et al. (2000) local starburst attenuation curve as the blue dashed line. The uvw2 and uvw1 filters can easily measure the UV slope of the observed attenuation curve, while uvm2 can constrain the UV bump strength.

BPT diagrams (Baldwin et al. 1981). For this work, the most relevant emission lines are H α and H β .

In order to simultaneously study NUV and optical properties, we cross-referenced the MaNGA Product Launch 7 (MPL-7), corresponding to the SDSS Data Release 15, or DR15 (Aguado et al. 2019), with the *Swift*/UVOT NUV archive as of April 26, 2018. UVOT is a 30-cm telescope that has a field of view (FOV) of $17' \times 17'$ with an effective plate scale of $1'' \text{ pixel}^{-1}$. The FWHM of the PSF varies across the NUV filters as reported in Table 1, but is around $2''.5$, similar to the angular resolution of the MaNGA data. The NUV UVOT filter transmission curves are displayed over representative attenuation and extinction curves in Figure 1. While both the uvw1 and uvw2 filters have small red leaks, this issue is unimportant here as we are targeting galaxies that exhibit strong star formation. The central wavelengths, bandpass FWHM, PSF FWHM, and the median and minimum exposure times for the observations of the galaxies in our sample are listed in Table 1. These exposure time statistics apply only to the star forming galaxies studied in this paper. While there is a significant range in total exposure times, all of these galaxies are bright and well detected, with a minimum S/N of 15 in both filters for the integrated galaxy light and 5 for that of the individual regions.

The UVOT detector is a microchannel plate intensified CCD that operates in a photon counting mode. As a result, bright sources can suffer from coincidence loss (as described in Poole et al. 2008; Breeveld et al. 2010). The objects in our sample are too faint for this to become a significant issue, as discussed in Section 3.2.

Since this project aims to study the NUV slope, we required that all objects in our sample have UVOT images in both the uvw1 and uvw2 filters. We place a secondary constraint on the X-ray emission, $L_X(2-10) \text{ keV} \lesssim 10^{41} \text{ erg s}^{-1}$, to exclude luminous active galactic nuclei (AGN), using the

Table 1. *Swift*/UVOT NUV Observation Properties

Filter	Central Wavelength ^{a, b} (Å)	FWHM ^a (Å)	PSF FWHM ^a (arcsec)	Median Exposure ^c (s)	Minimum Exposure ^c (s)
uvw2	1928	657	2.92	2375	277
uvm2 ^d	2246	498	2.45	2548	166
uvw1	2600	693	2.37	2296	279

^a The quoted filter properties are from Breeveld et al. (2010)

^b The central wavelength assumes a flat spectrum in f_ν .

^c The exposure time statistics are based on the subset of “star forming” galaxies defined by the criteria in Section 4.

^d The uvm2 exposure time statistics are calculated for the 25 star forming galaxies that have uvm2 images.

Swift X-ray Telescope (XRT) point source catalog (Evans et al. 2013). These requirements produce a sample of 139 galaxies. The median redshift of these objects is 0.03, which corresponds to a luminosity distance of $D_L = 130 \text{ Mpc}$ and a spatial scale of $600 \text{ pc}''$; this redshift is similar to the average for MaNGA galaxies ($\langle z \rangle \approx 0.037$). The stellar masses of the galaxies in the sample, obtained via spectral energy distribution (SED) fits from the NASA-Sloan Atlas (Blanton et al. 2011), span the range $8.73 \leq \log(M/M_\odot) \leq 11.11$. A full description of the total sample, which does not include the secondary constraint on the X-ray emission, is presented in Molina et al. (in preparation). From the sample of 139 galaxies, we select 29 galaxies with SFRs appropriate for our study. These criteria are described in detail in Section 4.1.

3 DATA REDUCTION

3.1 MaNGA Data Reduction

The MaNGA spectra are reduced using the MaNGA Data Reduction Pipeline (DRP; Law et al. 2016) which carries out the spectral extraction and calibration to produce datacubes. The datacubes are then processed through the MaNGA Data Analysis Pipeline (DAP; Westfall et al. 2019; Belfiore et al. 2019), which creates 2-D maps of measured emission line strengths and spectral indices, as well as the best-fitting model spectra for all pixels that were successfully fit. We use the reduction version from MPL-6, which is nearly identical to SDSS DR15. DAP fits the stellar continuum using a list of 42 average stellar spectral templates constructed from the MILES library (Sánchez-Blázquez et al. 2006) using a hierarchical clustering algorithm (see Westfall et al. 2019, for details). The fitting employs the Penalized Pixel-Fitting code (Cappellari & Emsellem 2004). For this work, we employ the “hybrid” binning scheme from the DAP, which is optimal for emission line measurements. This scheme involves a two-step fitting process. First the stellar continua of the Voronoi-binned spectra (Cappellari & Copin 2003) are fitted, with the resulting fit saved as a template. Then the emission lines in the individual pixels are fitted simultaneously with the stellar continuum, using the fixed template from the previous step. This process is carried out for each pixel to create 2-D maps of emission line flux across the face of the galaxy. Spectral indices such as the Balmer break, or $D_n(4000)$, are measured in the

Voronoi-binned spectra from the first step. As this project relies on spatial resolution, we recalculate the $D_n(4000)$ maps without Voronoi binning, using the continuum windows of $\lambda_{\text{blue}} = 3850\text{--}3950 \text{ \AA}$ and $\lambda_{\text{red}} = 4000\text{--}4100 \text{ \AA}$. The reported errors include the correction factors derived from repeat observations as described in Westfall et al. (2019); Belfiore et al. (2019): the flux errors are multiplied by 1.25, and the $D_n(4000)$ errors by 1.9. These correction factors reliably account for the random and systematic errors associated with varying conditions during the observations and the methods used to make the measurements. The stellar mass and SFR within 1 effective radius ($1 R_e$) quoted in Table 2 are drawn from the NASA-Sloan Atlas (Blanton et al. 2011) and MaNGA DAP, respectively.

3.2 *Swift*/UVOT Data Processing

The UVOT data are obtained from the High Energy Astrophysics Science Archive Research Center (HEASARC), and are processed using the *Swift* UVOT Pipeline¹, an updated and automated version of `uvot_deep.py`, which is a subroutine in UVOT Mosaic². These routines complete the basic data processing as described in the UVOT Software Guide³. Both the counts and exposure maps are aspect corrected, which reduces any uncertainty in the defined world coordinate system to $\sim 0''.5$. In order to ensure reliable final images, we require that all individual frames are 2×2 binned, which yields a plate scale of $1'' \text{ pixel}^{-1}$. UVOT images are composed of single frames, with very short exposure times, which are stacked together to create an image with the desired total exposure time. While different UVOT frame exposure times are possible, the UVOT software does not allow for the combination of different frame times as it complicates the image analysis. Therefore, we use the standard full frame time of 11.0322 ms.

All individual events in each UVOT frame are identified and the centroid of the event location is saved. The location of each event is placed into the final UVOT image, with each event stored as a count. A cosmic ray hitting the detector will register at most a few counts at a single location on the UVOT image rather than the thousands of counts expected from a relatively bright stationary source. Therefore, even though cosmic rays are non-uniform, they affect very few frames, and thus are incorporated into the background sky counts.

The resulting UVOT images were corrected for the dead time and the degradation of the detector. Approximately 2% of the full frame time is dedicated to transferring the charge out of the detector, which must be corrected by increasing the count rate (Poole et al. 2008). The decline in count rate measured by the UVOT NUV filters due to the degradation of the detector is well characterized and described in the UVOT calibration documents⁴, resulting in a 2.5% correction for the most recent observations.

As UVOT operates in photon-counting mode, coincidence loss can be a significant problem for bright sources. Coincidence loss occurs when two or more photons arrive at a similar location within the same frame, and their pile-up can affect the measured count rate. While Breeveld et al. (2010) describe coincidence loss for the case when a point source is superposed on some diffuse background (e.g., knots of star formation on top of diffuse galactic background), the spatial resolution of our data ($\sim 2 \text{ kpc}$) does not allow us to resolve individual H II regions. Therefore, that method is not appropriate; instead, we approached this problem using the prescription in Poole et al. (2008). Their formulated coincidence loss corrections are only valid for point sources, but the effect is only significant when the count rate is above $10 \text{ counts s}^{-1} \text{ pixel}^{-1}$. The UVOT observations of our sample have a maximum count rate of $< 0.9 \text{ counts s}^{-1} \text{ pixel}^{-1}$, translating to a correction of $\sim 0.6\%$, significantly smaller than the dead time correction of 2%. Therefore the effects of coincidence loss are negligible and we ignore them in this work. A full description of the *Swift*/UVOT data reduction and the *Swift* UVOT Pipeline is given in Molina et al. (in preparation).

3.3 *Swift*/UVOT Sky Subtraction

The final reduction step for the UVOT images was to subtract the local background sky emission. In order to identify the local background, we quantified the extent of each galaxy by calculating its Petrosian radius (1976) in the uvw2 filter, i.e., where the local intensity equaled 20% of the average flux contained within that aperture. The average Petrosian radius for our sample was $11''.9$, much smaller than the $17' \times 17'$ UVOT FOV. The sky annulus was defined with an inner radius of twice the calculated Petrosian radius and a set area of 1000 square arcseconds. We used the biweight estimator of the central location to estimate the sky counts. This estimation method was used to avoid the effect of any objects that fall within the sky annulus. The resulting sky counts were minimal as expected, and yield integrated magnitudes consistent with those from the *Galaxy Evolution Explorer* (GALEX; Martin et al. 2005, see Section 4.2.3 for details). We then calculated the background sky emission in the uvw1 filter via the same procedure; as there was at most a 1–2 pixel difference between the Petrosian radii calculated for uvw1 and uvw2, we simply adopted the uvw2 radius for this measurement.

3.4 Spatial Sampling and Resolution Matching of SDSS-IV/MaNGA Maps and *Swift* Images

While the NUV images from UVOT and the optical spectra from MaNGA have approximately the same angular resolution, the sampling is not the same. In order to directly compare the two data sets, the MaNGA 2-D maps must be re-sampled to the UVOT pixel size ($1'' \text{ pixel}^{-1}$, double that of MaNGA), and angular resolution. To do this, we adopt the resolution of the UVOT uvw2, which has the poorest spatial resolution (see Table 1). We first re-sample the 2-D MaNGA maps with a 2×2 top hat convolution kernel to match the UVOT pixel scale of $1''$. After re-sampling the maps, we change the angular resolution of the MaNGA

¹ github.com/malmolina/Swift-UVOT-Pipeline

² github.com/lea-hagen/uvot-mosaic

³ heasarc.gsfc.nasa.gov/docs/swift/analysis

⁴ heasarc.gsfc.nasa.gov/docs/heasarc/caldb/swift/docs/uvot

data cube to match that of uvw2 by employing a Gaussian convolution kernel of standard deviation σ_M such that $\sigma_{MaNGA}^2 + \sigma_M^2 = \sigma_{Swift}^2$. This process was completed for each 2-D MaNGA map and associated error image of interest. A full description of this process is presented in Molina et al. (in preparation).

4 PROPERTIES OF STAR FORMING GALAXIES

4.1 Identifying Star Forming Galaxies

While most of our galaxies have single-fiber SDSS spectra, about 45% of the objects in our sample do not have detailed classifications beyond “galaxy” in the SDSS DR15 release (see Bolton et al. 2012, for a description of the classification routine). Additionally, as this study focuses on understanding attenuation in galaxies, we wish to identify star forming galaxies in a reddening independent manner. To this end, we used the MaNGA integrated emission line flux maps to create masks based on BPT diagrams to determine the locations of star formation. We used the starburst models described in Kewley et al. (2006), which include the theoretical extreme starburst line described in Kewley et al. (2001), as well as the empirical line defining composite objects described in Kauffmann et al. (2003). We then used the MaNGA data to create maps of the reddening-insensitive diagnostic ratios $[O III]/H\beta$, $[N II]/H\alpha$, $[S II]/H\alpha$ and $[O I]/H\alpha$. These emission line ratio maps were used to create masks that identified pixels that were classified as star forming in all three of the $[O III]/H\beta$ vs. $[N II]/H\alpha$, $[S II]/H\alpha$ and $[O I]/H\alpha$ diagrams. For the $[O III]/H\beta$ vs. $[N II]/H\alpha$ diagram, we additionally required that the measured emission line ratios were not in the composite object region defined by Kauffmann et al. (2003).

The masks were used to identify galaxies where a large majority of the pixels, especially in the nuclear and circum-nuclear regions, are star forming according to all three BPT diagrams. We identified 29 galaxies that satisfied these criteria and verified that none of these objects have an SDSS classification of AGN. We then confirmed that the 29 objects selected were indeed star forming galaxies by plotting their locations in the SFR–stellar mass plane against the entirety of the MaNGA sample as shown in Figure 2. Almost all of the galaxies in our sample fall on or above the cloud of star forming galaxies. Their SFRs within $1 R_e$, $SFR_{1R_e}(H\alpha) \lesssim 10 M_\odot \text{ yr}^{-1}$, are well under the maximal value of those studied by B16 ($SFR[H\alpha] \lesssim 40 M_\odot \text{ yr}^{-1}$), making their star forming galaxy attenuation law more appropriate than the Calzetti et al. (2000) starburst law. We therefore conclude that these galaxies are star forming, not subject to AGN contamination, and are appropriate for the proposed analysis. This final sample of galaxies has similar properties to that of B16: their stellar masses are in the range $8.76 \leq \log(M_*/M_\odot) \leq 10.7$ with a median of 9.65, and their SFRs are in the range $-1.52 \leq \log[SFR_{1R_e}(H\alpha)/(M_\odot \text{ yr}^{-1})] \leq 0.94$ with a median of -0.45 . However, the sample is dominated by objects with lower stellar masses and SFRs; 69% of the galaxies have $\log(M_*/M_\odot) \leq 10.0$, while 76% have $SFR_{1R_e}(H\alpha) \leq 1 M_\odot \text{ yr}^{-1}$. The stellar mass, SFRs, and other basic properties for

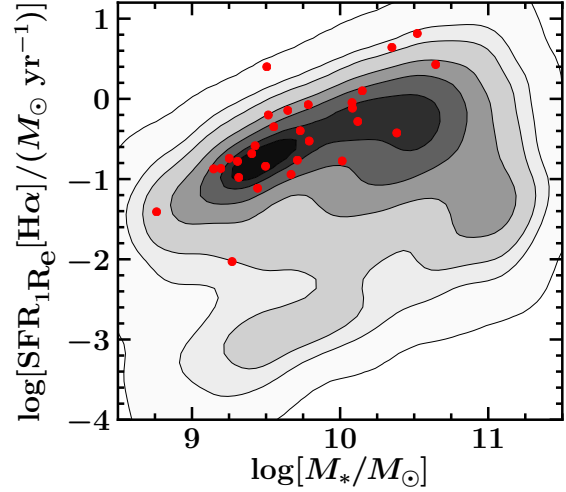


Figure 2. The SFR within $1 R_e$ vs. stellar mass for the 29 star forming galaxies in the sample (red filled squares), overlaid on the full MaNGA sample (black and grey contours). The contours represent fractional values of the maximum number density, with lines of constant number density drawn at the 90%, 80%, 60%, 40%, 20%, 10% and 1% levels. The galaxies studied in this work primarily fall on or above the star forming cloud. The stellar mass measurements are from the NASA-Sloan Atlas (Blanton et al. 2011), and the SFR is calculated within 1 effective radius using the $H\alpha$ map from the MPL-6 version of the MaNGA DAP (Westfall et al. 2019), after applying an internal reddening correction using the O’Donnell (1994) Milky Way extinction curve.

the star forming galaxies in our sample are listed in Table 2.

4.2 Attenuation in Integrated Light of Star forming and Starburst Galaxies

To employ the B16 approach to study attenuation, we must assume that the UV stellar continuum is well described by a power law of the form $F_\lambda(\lambda) \propto \lambda^\beta$. Here $F_\lambda(\lambda)$ is the observed flux density per unit wavelength, and the power-law index (or slope in log space) is β . We are interested in vigorously star forming galaxies as we expect their integrated light will generally follow the relation between optical nebular and UV stellar continuum attenuation described by either Calzetti et al. (1994) or B16. We confirmed this behavior by measuring the τ_B^l and β of the integrated NUV stellar continua and optical nebular light for all galaxies in the sample, as described in Sections 4.2.1 and 4.2.3. For consistency with previous analysis, we then compare the values of β calculated using the *Swift* NUV filters to those derived from the GALEX FUV and NUV filters, as described in Section 4.3. In cases where the galaxy was face-on, the circular uvw2 Petrosian radius (1976), described in Section 3.3, is adopted. If the galaxy was edge-on, or very elongated, an elliptical aperture that traced the majority of the measured $H\alpha$ flux was used. We compared the measured apparent magnitude of the integrated light in the uvm2 filter, when available, to the apparent NUV magnitude from GALEX measurements. All the uvm2 apparent magnitudes agreed with those from the GALEX NUV filters within the error, i.e., $|m_{\text{uvm2}} - m_{\text{GALEX}}| \lesssim 0.1$, and $\langle |m_{\text{uvm2}} - m_{\text{GALEX}}| \rangle = 0.03$.

The typical errors for the apparent uvm2 and GALEX magnitudes are 0.06 and 0.08, respectively.

4.2.1 Calculating the Integrated τ_B^I

Calzetti et al. (1994) and B16 follow the same general procedure to develop their attenuation laws: they measure the relation between the UV spectral slope and Balmer optical depth for the integrated light of galaxies and plot them against each other to quantify the difference in colour excess between the UV stellar and optical nebular emission. The calculation of τ_B^I is carried out via

$$\tau_B^I = \tau_\beta - \tau_\alpha = \ln\left(\frac{f(\text{H}\alpha)/f(\text{H}\beta)}{2.86}\right), \quad (1)$$

where 2.86 is the theoretical value for Case B recombination in a low density, $T = 10^4$ K plasma (Osterbrock & Ferland 2006, Section 4). τ_B^I is defined to be independent of the assumed extinction law. When $\tau_B^I = 0.0$ the measured Balmer decrement is equal to the intrinsic value and there is assumed to be no dust in the system. Therefore, if the assumed star formation history (SFH) is correct and the sightline coverage of both the nebular emission and UV stellar continuum by the attenuating dust are identical, the value of β at $\tau_B^I = 0.0$ is also the intrinsic UV spectral slope of the stellar continuum. Any offset in β at $\tau_B^I = 0.0$ in the B16 relation would then be a result of the SFH and/or the geometry of the attenuating dust, the stars and the gas (see B16; Calzetti 2013; Calzetti et al. 2015, for discussions on this topic).

We calculated the integrated τ_B^I by using the observed H α and H β MaNGA flux maps. The integrated emission was defined as all valid pixels that fall within both the MaNGA IFU footprint and the apertures used to compare uvm2 measurements to GALEX measurements, regardless of whether the emission was dominated by star formation according to BPT diagrams. We define valid pixels as all pixels that are not flagged as untrustworthy by the MANGA DAP (see Westfall et al. 2019, for details). The same apertures and masks were used for the integrated UV spectral slope (β) measurement, for consistency. The larger aperture will introduce scatter between the integrated light and individual regions, which will be explored in Section 7. All maps from MaNGA are corrected for foreground extinction by the MaNGA DAP, using the values from Schlegel et al. (1998) listed in Table 2, and assuming the O'Donnell (1994) Milky Way dust extinction curve with $R_V = 3.1$.

4.2.2 UVOT Foreground Extinction Correction

The NUV foreground extinction corrections were calculated using a multistep process. We began by combining the Fitzpatrick (1999) Milky Way extinction curve assuming $R_V = 3.1$ and a range of $E(B - V)$ values, with each of the 13 solar metallicity, continuous star forming SEDs from Starburst99 (Leitherer et al. 1999). The resulting SEDs were multiplied by the appropriate filter curve and integrated over all wavelengths. We calculated an average total-to-selective extinction, $k(\lambda) \equiv A_\lambda/E(B - V)$, for the two filters: $k_{\text{uvw1}} = 6.269$ and $k_{\text{uvw2}} = 8.069$. The stellar age of the SED did not significantly increase the scatter in the $k(\lambda)$ calculation; the choice in extinction law (i.e., Cardelli et al. 1989; Fitzpatrick 1999;

O'Donnell 1994) was the dominant source of uncertainty. We employed the Fitzpatrick extinction law for two reasons: (1) this extinction law is the same used in B16, and (2) this law has a thorough, careful treatment of the UV light. The difference in the total-to-selective extinction between the different extinction laws is $k_{\text{uvw1}, \text{Fitzpatrick}} = 0.9k_{\text{uvw1}, \text{O'Donnell}}$ and $k_{\text{uvw2}, \text{Fitzpatrick}} = 0.98k_{\text{uvw2}, \text{O'Donnell}}$. When assuming the maximal $E(B - V)$ value for the objects in our sample, the foreground extinction-corrected colour $\text{uvw2} - \text{uvw1}$ when assuming the Fitzpatrick law is 0.03 mag larger than when assuming the O'Donnell law. We note this systematic offset but do not include it in our calculated errors, especially as it is negligible compared to the systematic uncertainty associated with the transformation of β as described in Section 4.3. Finally, as we are only interested in the power-law slope of the UV stellar continuum using the $\text{uvw2} - \text{uvw1}$ colour, there is no need to perform K-corrections on the flux density.

4.2.3 Calculating the Integrated β_{Swift}

Calculating β is a more complex, object-specific process than that for τ_B^I , and is complicated by the fact that we do not know the shape of the intrinsic spectrum. The B16 relation relied on the work first done by Calzetti et al. (1994), which used spectra covering a wavelength range of 1200–3200 Å. Calzetti et al. (1994) used 10 continuum windows in the UV spectrum to calculate β , while B16 and this work use colours from GALEX and UVOT, respectively. Fortunately, our sample has very similar properties to that of B16 (see Table 2 in B16), so we calculated β_{Swift} in a similar manner, as described below.

We started with the 100 Myr continuous star formation stellar continuum model generated by Starburst99 (Leitherer et al. 1999), which assumes a constant SFR of $1 M_\odot \text{ yr}^{-1}$. This model was chosen for consistency with B16, who note that the exact age of the reference spectrum is less important than the assumption of a continuous SFR. Thus we assume a nominal intrinsic, unreddened $\beta_0 = -2.38$ (Calzetti 2001). This choice will have consequences on our β calculations, which will be discussed in detail in Section 4.4.

The 100 Myr continuous star formation SED was redshifted according to the recessional velocity of each object. We then reddened the resulting model using the B16 attenuation law for a range of $E(B - V)$ values. For each reddened SED, we measured the UV spectral slope via the same continuum windows used by Calzetti et al. (1994), and also calculated the UVOT $\text{uvw2} - \text{uvw1}$ colour. We then used the measured β_{Swift} values as a function of UVOT colour to calculate the integrated galaxy β_{Swift} measurements for the objects in our sample. Finally, we compared the β_{Swift} values to GALEX β measurements using the process described in Section 4.3. The integrated β and τ_B^I for the sample are given in Table 2, with the exception of NGC 3191, where the MaNGA observations do not cover a significant portion of the galaxy disc. The difference in the uvw1 and uvw2 Petrosian radii is unimportant for this study as we are limited by the MaNGA FOV and pixel masks, as described in Section 4.2.1.

4.3 Conversion of β from UVOT to GALEX

While the calculations described in Section 4.2.3 are consistent with the methodology described in B16, our baseline is restricted to the wavelength range between $\sim 2000 \text{ \AA}$ and $\sim 2600 \text{ \AA}$, i.e., the NUV, while B16 used the GALEX NUV and FUV filters. Thus, there could be a systematic offset between β_{Swift} and β values obtained using entire UV wavelength range (see Appendix B in Calzetti 2001, for a complete discussion). In short the “iron curtain” at longer UV wavelengths can depress the continua in the NUV, giving UV slopes with shorter baselines more negative values. They found that the relationship between the two β values in UV-selected starbursts is linear, with a slope of order unity. Meanwhile, Meurer et al. (1999) found a constant, negative offset between UV slopes calculated with longer and shorter wavelengths, such that the short-wavelength slope is bluer.

In order to provide a more faithful comparison to B16, we compare our β_{Swift} values with UV slopes calculated with GALEX. To do this, we measured integrated, aperture-matched magnitudes from both the NASA-Sloan Atlas and our Swift archival data (full details described in Molina et al. in preparation) using the r -band elliptical aperture from the NASA-Sloan Atlas, corrected for inconsistencies in the PSFs of the instruments.

β_{GALEX} is calculated via the method used to calculate β_{IUE} described in B16, while the β_{Swift} is calculated as described in Section 4.2.3. We only include objects that: (1) have GALEX detections in both bands with $\sigma_{\text{m,GALEX}} < 0.5 \text{ mag}$, (2) have an axial ratio $b/a > 0.42$ (this will minimize contamination by the 2175 \AA bump as described in Battisti et al. 2017), and (3) have $D_n(4000) \lesssim 1.4$ to create a sample similar to that in B16. The resulting relation between β_{Swift} and β_{GALEX} is shown in Figure 3, and is well-fit with a linear model of the form

$$\beta_{\text{GALEX}} = (0.9 \pm 0.3)\beta_{\text{Swift}} - (0.2 \pm 0.3), \quad (2)$$

with a scatter about the relation of $\sigma_{\text{disp}} = 0.2$. Therefore, while we find a similar result to that of Calzetti (2001) and Meurer et al. (1999), the large dispersion drives the overall observed uncertainty in this relation. Furthermore, we have no robust way to differentiate between the systematic and random components associated with that dispersion. As the two β values are statistically equivalent given the errors on the fitted parameters, we do not transform β_{Swift} . However, to account for this observed dispersion between the GALEX and Swift-calculated β values, we adopt an additional uncertainty of $\sigma = 0.2$ into our error bar. This transformation is the largest source of uncertainty in the β error budget.

4.4 Continuous vs. instantaneous star formation

Our calculation of β assumes a continuous SFH instead of an instantaneous burst; this is significant, as β is highly dependent on the intrinsic slope and thus on the assumed SFH. To quantify the difference between the two families of models, we measured β in the same manner described in Section 4.2.3 and compared the UVOT colour and intrinsic β for instantaneous burst and continuous star formation stellar continua generated by **Starburst99** (Leitherer et al. 1999). The two families of models agree for $\beta \lesssim -1.8$, which translates to an age of $\sim 50\text{--}100 \text{ Myr}$ (Calzetti 2001).

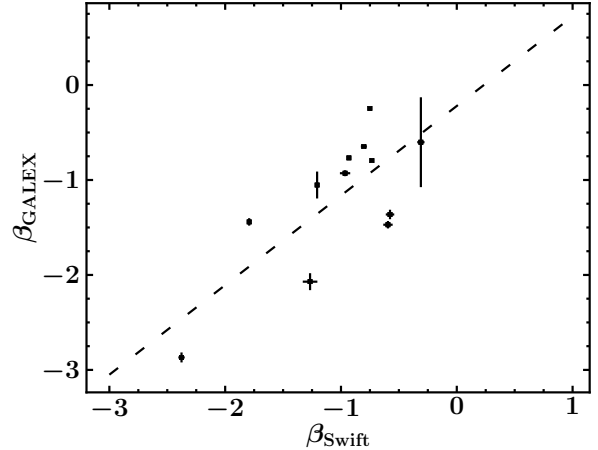


Figure 3. Comparison of the UV spectral slope (β) as computed with GALEX and *Swift* data. We only include objects with uncertainties in both GALEX and *Swift* filters less than 0.5 mag, an axial ratio $b/a > 0.42$, and $D_n(4000) \lesssim 1.4$. The resulting fit is given by Equation 2, but the uncertainty in this relation is driven by the dispersion, $\sigma_{\text{disp}} = 0.2 \text{ mag}$. To account for this, we adopt an additional uncertainty of $\sigma = 0.2$ in our calculation of β .

However for more realistic SFHs, rapid changes in the SFH could easily affect the measured β . For example, a SFH with an exponential decay and a short e-folding time would produce a sharp increase in β shortly after the initial burst. Thus, unless we caught the burst very close to its onset, the calculated β values under this assumption would be systematically too blue for such a system.

We have tried to minimize this effect by selecting galaxies that exhibit strong $\text{H}\alpha$ emission ($\langle \Sigma_{\text{H}\alpha} \rangle \gtrsim 10^{38} \text{ erg s}^{-1} \text{ kpc}^{-2}$), which implies that they have undergone vigorous star formation within the last 10 Myr (Kennicutt & Evans 2012). In addition, we confirm that most of the galaxy has nebular emission consistent with star formation; this avoids galaxies undergoing quenching. Finally, while our presented β values for the individual galaxies and kpc-sized regions may be systematically offset from their true value, we emphasize that the galaxies have similar mass, and both the galaxies and regions identified are currently forming stars at a similar rate to those presented in B16. Therefore, as with B16, the distribution of the sample about the assumed intrinsic β should be reliable.

4.5 Effects of Stellar Age, the 2175 \AA bump, and S/N on β

Figure 4 compares the relation from B16 to the integrated β and τ_B^I from the 29 galaxies in our sample. The gray shaded bar represents the sample dispersion from B16, which is larger than the error associated with the fit. Both B16 and this work probe stellar age using as a proxy the $D_n(4000)$ index, which samples the 4000 \AA break (Balogh et al. 1999). This feature is produced by the absorption of light by metals in the atmospheres of cool stars, and is thus stronger in older stellar populations; younger systems have stronger UV fluxes, which dilute this break. For our purposes, we consider $D_n(4000)$ as an indication of the relative contribution of older stars compared to younger stars. The $D_n(4000)$ values pre-

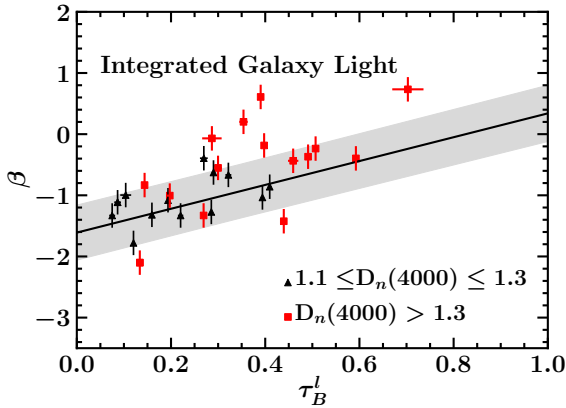


Figure 4. The UV spectral slope (β) vs. the Balmer optical depth (τ_B^l) of the integrated galaxy light from our 29 galaxies, compared to the relation reported in B16 (solid black line). The grey shaded region represents the sample dispersion of the B16 relation, which is larger than the error in the fitted model. B16 only considered galaxies with $1.1 \leq D_n(4000) \leq 1.3$ when deriving the relation between β and τ_B^l . The symbols represent galaxies with different $D_n(4000)$ values: the black triangles denote galaxies with $1.1 \leq D_n(4000) \leq 1.3$, and the red squares represent redder systems with $D_n(4000) > 1.3$. Galaxies with larger $D_n(4000)$ lie preferentially above the fitted relation, consistent with the trends seen in B16.

sented in this work are measured using the MaNGA maps, and represent the integrated value within the aperture.

B16 focused on the unresolved nuclear regions of galaxies, with scales similar to the individual regions we study in detail starting in Section 5. We find qualitatively that the integrated light in star forming galaxies follows the same relation as their nuclear regions. We will explore the change in attenuation across the galaxy and the effect of aperture size in Section 7.

The integrated light for all of the galaxies in our sample have $D_n(4000)$ measurements smaller than the upper limit in the full B16 sample. However, B16 based their fitted relation on galaxies with $1.1 \leq D_n(4000) \leq 1.3$. They do note that the values of β and τ_B^l tend to increase with $D_n(4000)$, which is consistent with our findings. As clearly demonstrated, the integrated light from our sample, on average, has a higher $D_n(4000)$ value than the galaxies used to define the fitted B16 relation. However, the UV light from the individual star forming regions should be dominated by massive, young stars; therefore, we will consider the entirety of the sample.

For this project, we assume that our galaxies are similar to those studied by B16, which themselves were further explored by Battisti et al. (2017). They found that galaxies with $b/a < 0.42$ show evidence of a 2175 \AA bump in their attenuation curves. We only have 3 such objects in our sample, and do not see any systematic trends with inclination in the integrated light. In addition to these physical effects, we explored the effect of the large range in the signal-to-noise (S/N) ratio on our measurement of β . We do not see any strong systematic trends with the measured S/N in either filter with respect to the measured β in the integrated aperture.

5 KILOPARSEC-SCALE STAR FORMING REGIONS

5.1 Isolating Individual Regions

The combination of the kpc-scale spatial resolution of our data and the diffuse galaxy light severely restricts the effectiveness of most commonly used methods for the identification of star forming regions (e.g., Source Extractor; Bertin & Arnouts 1996). Instead, we used the dereddened $H\alpha$ surface brightness maps ($\Sigma_{H\alpha}$) in combination with BPT diagrams and the $H\alpha$ equivalent width, $EW(H\alpha)$, to define the kpc-sized regions of star formation. While $\Sigma_{H\alpha}$ measurements do require a correction for internal attenuation, all attenuation curves yield approximately the same correction at $H\alpha$, making it the most robust tracer of recent star formation. To create our sample of star forming regions, we began by selecting an initial minimum $H\alpha$ surface brightness of $\log[\Sigma_{H\alpha}/(\text{erg s}^{-1} \text{ kpc}^{-2})] = 39$; this threshold prevented excessive contamination from diffuse ionized gas (DIG) in the defined region. Such contamination is ubiquitous on MaNGA spatial scales as described in Zhang et al. (2017), but they recommend a limit of $\log[\Sigma_{H\alpha}/(\text{erg s}^{-1} \text{ kpc}^{-2})] = 39$ to identify *pixels* dominated by light from the $H II$ regions; in contrast pixels with $\log[\Sigma_{H\alpha}/(\text{erg s}^{-1} \text{ kpc}^{-2})] < 38$ are dominated by DIG. This means that all of the regions we identify in the first pass meet this strong constraint.

While subtraction of the diffuse galaxy component would allow us to exclude light from older stellar populations, the observed spatial scale does not allow us to cleanly identify individual $H II$ regions. Therefore, any “diffuse component” we measure could have low levels of star formation, which could impact the measured β . We thus decided not to subtract out the diffuse component from our measurements. To mitigate the presence of a large diffuse component, we also required that the mass-specific SFR proxy $EW(H\alpha) > 15 \text{ \AA}$. This step is done after defining our individual regions to identify those that are “DIG-dominated”. Finally, to avoid any potential uncertainties due to the difference in the PSF between uvw1 ($2''.37$) and uvw2 ($2''.92$), we adopt a minimum aperture diameter of $5''$.

Using a combination of BPT and $\Sigma_{H\alpha}$ diagnostics, we iteratively identified the kpc-size star forming regions using the following four step process:

(i) Identify local peaks where the observed, reddening-corrected $H\alpha$ surface brightness is $\log[\Sigma_{H\alpha}/(\text{erg s}^{-1} \text{ kpc}^{-2})] \geq 39$, and confirm they are separated by at least $5''$ (corresponding to the diameter of two resolution elements). Both foreground and internal reddening corrections assume the O’Donnell (1994) Milky Way dust extinction curve, and $R_V = 3.1$. The choice of attenuation law did not affect the value of $\Sigma_{H\alpha}$ within our measurement errors.

(ii) Define the largest isophotal contour that corresponds to $\log[\Sigma_{H\alpha}/(\text{erg s}^{-1} \text{ kpc}^{-2})] \geq 39$ and separates the local $\Sigma_{H\alpha}$ peaks. If the contour has a diameter less than $5''$, adopt a circular aperture of that diameter. The contour or assumed circular aperture is then defined as a star forming region.

Table 2. Basic Properties of Star Forming Galaxies and UVOT images

Object I.D.	Object Name	SDSS Class. ^a	z^b	$E(B-V)_G^c$	b/a^b	R_{pet}^d (arcsec)	$\log(M_*)^e$ (M_\odot)	$\log(SFR)^f$ ($M_\odot \text{ yr}^{-1}$)	t_{uvw2} (s)	t_{uvw1} (s)	f_{lim}^g (uvw2)	f_{lim}^g (uvw1)	Σ_{uvw2}^h	Σ_{uvw1}^h	uvw2 ⁱ (mag)	uvw1 ⁱ (mag)	$\tau_{B,int}^l$ ^{j,k}	$\beta_{int}^{j,l}$
1	UGC 11696 NOTES01	SF	0.017	0.101	0.52	16	8.76	-1.23	1439	816	5.7	7.0	2.3±0.1	1.8±0.1	18.31±0.03	18.15±0.07	0.075±0.006	-1.3±0.2
2	SDSS J170653.67+321010.1	SF	0.036	0.039	0.82	15	9.15	-0.68	1420	6283	5.2	1.3	0.84±0.03	0.63±0.01	18.81±0.04	18.59±0.02	0.086±0.008	-1.1±0.2
3	WISE J162856.63+393634.1	SF	0.035	0.010	0.48	9	9.19	-0.62	8412	5674	1.2	1.3	1.91±0.04	1.49±0.03	19.85±0.02	19.44±0.02	0.270±0.009	-0.4±0.2
4	2MASS J04072365-0641117	SF	0.038	0.098	0.60	18	9.25	-0.71	788	1785	8.9	3.8	1.2±0.1	0.72±0.03	18.68±0.06	18.71±0.04	0.134±0.005	-2.1±0.2
5	2MASX J11044509+4509238	SF	0.022	0.008	0.88	6	9.27	-1.52	2265	13689	3.8	0.8	2.5±0.1	2.17±0.04	20.81±0.06	20.31±0.02	0.29±0.03	-0.1±0.2
6	2MASS J14135887+4353350	SB	0.040	0.013	0.71	7	9.31	-0.61	2066	1048	3.5	4.8	5.1±0.2	3.5±0.1	19.42±0.03	19.13±0.04	0.144±0.005	-0.8±0.2
7	KUG 1016+468	SF	0.024	0.013	0.45	13	9.32	-0.87	10027	2296	1.4	2.8	3.72±0.04	2.54±0.05	18.66±0.01	18.41±0.02	0.197±0.006	-1.0±0.2
8	SDSS J030659.79-004841.5	SF	0.038	0.070	0.78	8	9.40	-0.61	4084	3567	2.5	2.4	3.66±0.08	2.56±0.07	18.93±0.03	18.76±0.03	0.220±0.006	-1.3±0.2
9	2MASS J14132780+4354501	SF	0.040	0.013	0.40	13	9.43	-0.56	2066	1048	3.5	4.8	2.81±0.06	1.76±0.06	18.82±0.02	18.65±0.03	0.159±0.004	-1.3±0.2
10	SDSS J024112.93-005236.9	SF	0.038	0.034	0.56	10	9.44	-1.07	20519	3474	0.7	2.2	1.29±0.02	0.97±0.03	19.18±0.02	18.93±0.03	0.10±0.01	-1.0±0.2
11	2MASS J15004786+4836270	SF	0.037	0.020	0.54	7	9.50	-0.54	2108	1579	4.0	3.8	2.3±0.1	2.0±0.1	20.60±0.07	20.04±0.06	0.354±0.009	0.2±0.2
12	2MASX J0740537+400411	N/A	0.042	0.052	0.59	9	9.50	0.47	4558	3904	2.3	2.2	17.7±0.1	10.9±0.1	16.83±0.03	16.78±0.01	0.120±0.009	-1.8±0.2
13	KUG 0757+468	SF	0.019	0.065	0.53	14	9.52	-0.03	559	279	12.0	18.0	5.7±0.1	4.2±0.1	16.78±0.02	16.55±0.04	0.194±0.001	-1.1±0.2
14	2MASX J14403849+5328414	SB	0.038	0.011	0.80	8	9.55	-0.12	7621	1314	1.4	4.2	1.18±0.04	1.21±0.08	20.65±0.03	19.98±0.07	0.390±0.004	0.6±0.2
15	KUG 0254-004	SF	0.029	0.066	0.80	10	9.65	0.00	2375	2307	3.6	2.7	8.2±0.1	5.77±0.07	17.29±0.01	17.10±0.01	0.286±0.001	-1.3±0.2
16	2MASX J07522873+4950192	SF	0.022	0.059	0.50	30	9.67	-0.86	946	473	7.0	10.0	0.95±0.05	0.87±0.05	18.60±0.05	18.23±0.07	0.300±0.008	-0.6±0.2
17	KUG 0751+485	SB	0.022	0.035	0.71	5	9.71	-0.46	726	2669	9.0	2.8	1.06±0.06	0.90±0.03	19.37±0.06	18.91±0.03	0.398±0.001	-0.2±0.2
18	2MFGC 8582	SF	0.025	0.014	0.33	22	9.73	-0.23	4106	1017	2.0	4.6	1.81±0.05	1.65±0.07	19.43±0.03	19.02±0.05	0.593±0.005	-0.4±0.2
19	2MASX J07595878+3153360	SB	0.045	0.048	0.57	8	9.78	0.08	1402	1544	5.7	4.7	4.4±0.2	3.1±0.1	19.00±0.04	18.75±0.04	0.394±0.004	-1.0±0.2
20	KUG 1121+239	SF	0.028	0.019	0.80	14	9.79	-0.45	277	346	22.0	16.0	3.7±0.2	2.5±0.1	17.82±0.03	17.65±0.06	0.269±0.004	-1.3±0.2
21	WISE J163226.31+393104.0	SF	0.029	0.009	0.87	10	10.0	-0.53	994	599	7.1	7.9	1.22±0.06	0.97±0.05	19.15±0.05	18.75±0.05	0.46±0.01	-0.4±0.2
22	2MASX J09115605+2753575	SB	0.047	0.028	0.48	6	10.1	0.17	495	644	12.0	8.4	4.3±0.2	3.2±0.1	18.64±0.05	18.35±0.04	0.410±0.004	-0.9±0.2
23	KUG 1343+270	SF	0.030	0.017	0.54	21	10.1	-0.22	2998	6144	2.7	1.3	4.33±0.07	3.27±0.04	18.36±0.02	18.02±0.01	0.290±0.004	-0.6±0.2
24	2MASX J11532094+5220438	SF	0.049	0.029	0.87	10	10.1	0.00	2481	7471	2.9	1.1	3.10±0.06	2.35±0.03	18.95±0.02	18.61±0.01	0.327±0.006	-0.7±0.2
25	KUG 1626+402	SF	0.026	0.009	0.70	5	10.2	0.15	13227	8908	1.1	1.1	4.71±0.02	3.38±0.01	18.80±0.01	18.38±0.01	0.491±0.004	-0.4±0.2
26	NGC 3191 ^m	SF	0.031	0.011	0.86	17	10.3	0.73	11850	2296	1.3	2.9	24.06±0.04	10.10±0.05
27	LCSB S1611P	Galaxy	0.056	0.010	0.40	4	10.4	-0.13	12190	7209	1.0	1.2	0.50±0.02	0.53±0.02	20.90±0.04	20.20±0.04	0.70±0.04	0.7±0.2
28	2MASX J07333599+4556364	SF	0.077	0.091	0.89	11	10.5	0.94	3453	2048	2.5	3.4	3.40±0.07	3.21±0.08	18.62±0.02	18.16±0.03	0.507±0.003	-0.2±0.2
29	2MASX J03065213-0053469	SF	0.084	0.070	0.88	11	10.7	0.56	4084	3567	2.4	2.3	2.97±0.05	2.06±0.04	18.30±0.02	18.15±0.02	0.439±0.006	-1.4±0.2

^a The SDSS Classification of the galaxy (Bolton et al. 2012). SB stands for starburst, while SF stands for star forming galaxy.

^b The redshift and b/a values are taken from the NASA-Sloan Atlas (<http://nsatlas.org>; Blanton et al. 2011).

^c The foreground extinction measurements are from Schlegel et al. (1998).

^d The Petrosian Radii are calculated using the uvw2 filter as described in Section 3.3.

^e Stellar masses are taken from the SED fits from the MaNGA DRP (Law et al. 2016).

^f The SFRs within $1 R_e$ using the $H\alpha$ luminosity are drawn from the MaNGA Data Analysis Pipeline (Westfall et al. 2019).

^g f_{min} represents the minimum flux density detections, in units of $10^{-18} \text{ erg s}^{-1} \text{ cm}^{-2} \text{ \AA}^{-1}$, for a point source with a diameter of $2''.5$ at the redshift of the galaxy with a $S/N = 3$

^h The UV surface densities are given in units of $10^{-18} \text{ erg s}^{-1} \text{ cm}^{-2} \text{ \AA}^{-1} \text{ arcsec}^{-2}$, and are calculated by dividing the integrated, observed fluxes by the area of the integrated aperture.

ⁱ The uvw2 and uvw1 magnitudes are presented in the AB magnitude system without K-corrections.

^j The Balmer optical depth (τ_B^l) and UV spectral slope (β) are for the integrated light in the galaxy, See Section 4.2.3 for details.

^k The systematic uncertainty in the emission line flux as described by Belfiore et al. (2019) is included in the reported error. See Section 3.1 for details.

^l The systematic uncertainty of 0.03 mag due to choice in foreground attenuation curves is not included in these 1σ errors, as the $\beta_{Swift}-\beta$ “conversion” dominates the error budget. See Section 4.3 for details.

^m The MaNGA IFU does not cover a majority of the galaxy disc, so no $\tau_{B,int}^l$ and β_{int} are reported.

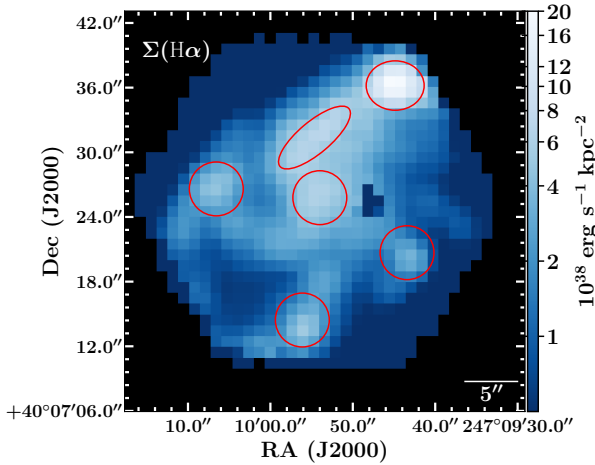


Figure 5. An example of the identified star forming regions in KUG 1626+402. The map displays the $H\alpha$ surface brightness across the face of the galaxy within the MaNGA FOV, and increases in intensity from dark blue to white as indicated by the colour bar. The angular resolution of the image is $\approx 2''$. A scale bar of $5''$ is shown on the lower right, corresponding to a physical scale of 2.61 kpc. The identified star forming regions are represented by the red circles and ellipses. Six regions were identified in this galaxy. See Appendix A, which is available online, for more information.

(iii) Confirm the nebular emission line ratios from the defined region fall within the star forming locus in all three BPT diagrams described in Section 4.1.

(iv) Repeat steps 1–3, stopping at a threshold of $\log[\Sigma_{H\alpha}/(\text{erg s}^{-1} \text{ kpc}^{-2})] \geq 38$ in increments of 0.2 in $\log(\Sigma_{H\alpha})$, while ensuring no region is identified more than once.

By iterating this process, we ensure that all peaks with $\log[\Sigma_{H\alpha}/(\text{erg s}^{-1} \text{ kpc}^{-2})] > 38$ are identified. The $\log(\Sigma_{H\alpha})$ limits exclude excessive amounts of DIG from the aperture, as the kpc-scales probed here do not allow for its clean subtraction. An example of the identified star forming regions for KUG 1626+402 is presented in Figure 5. We present the individual region positions and a full suite of images in Appendix A, which is available online.

Since we are interested in comparing “starburst”-like regions to normal star forming regions and are resolving kpc-sized regions instead of relying on pixels, we classify our regions using a combination of the criteria from Oey et al. (2007), Zhang et al. (2017), Sánchez et al. (2014) and Wang et al. (2018). We define a starburst region as one with $\log[\Sigma_{H\alpha}/(\text{erg s}^{-1} \text{ kpc}^{-2})] \geq 39.4$, while a normal star forming region has $38.0 < \log[\Sigma_{H\alpha}/(\text{erg s}^{-1} \text{ kpc}^{-2})] \leq 39.4$ and $\text{EW}(H\alpha) > 15 \text{ \AA}$. This is similar to the criterion for “star forming” regions defined by Oey et al. (2007), but combines the slightly lower $\Sigma_{H\alpha}$ cut presented in Zhang et al. (2017), and requires more than double the $\text{EW}(H\alpha) > 6 \text{ \AA}$ cut used by Sánchez et al. (2014) and Wang et al. (2018) to define star forming regions. Thus our regions appear star forming to both our area- and mass-specific SFR proxies. For regions that do not meet both of these criteria, the UV continuum may not be dominated by the light from massive stars; hence the assumptions behind the calculation of β may not hold. All such regions which were selected to meet the BPT constraints for a star forming region, but have ei-

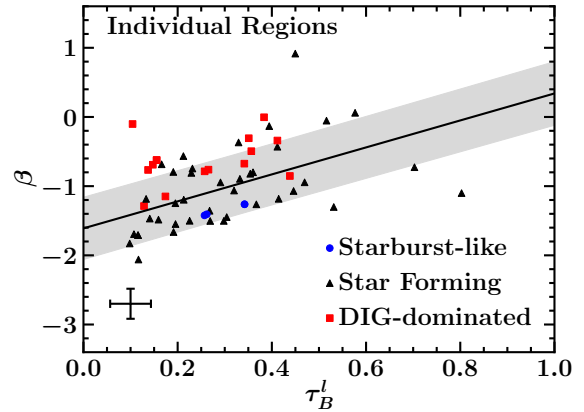


Figure 6. The UV spectral slope (β) vs. the Balmer optical depth (τ_B^l) of the individual star forming regions in our sample. The blue circles are starburst-like regions ($\log[\Sigma_{H\alpha}/(\text{erg s}^{-1} \text{ kpc}^{-2})] \geq 39.4$) and the black triangles are normal star forming regions ($38.0 < \log[\Sigma_{H\alpha}/(\text{erg s}^{-1} \text{ kpc}^{-2})] \leq 39.4$ and $\text{EW}(H\alpha) > 15 \text{ \AA}$), as defined in Section 5.1. The red squares are regions likely dominated by DIG ($\log[\Sigma_{H\alpha}/(\text{erg s}^{-1} \text{ kpc}^{-2})] < 38.0$ or $\text{EW}(H\alpha) < 15 \text{ \AA}$; see Section 5.1 for discussion). The error bar on the lower left represents the characteristic uncertainties in β and τ_B^l . The relation between β and τ_B^l from B16 is indicated by the solid black line, while the intrinsic dispersion of their data is shown by the grey shaded region.

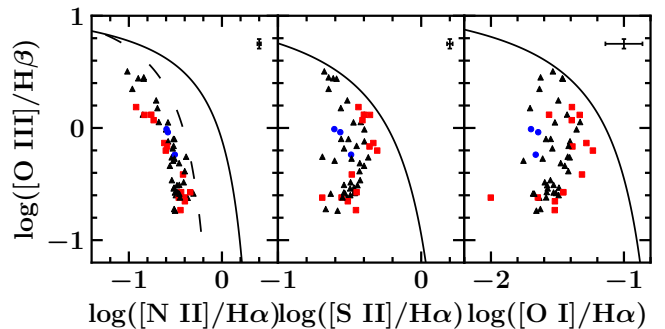


Figure 7. BPT diagrams for the individual star forming regions in our sample. The colour coding for the data is the same as in Figure 6. The solid black line in each panel is the extreme starburst limit from Kewley et al. (2006); the dashed line is the composite object locus from Kauffmann et al. (2003). All regions fall inside the star forming region of all three diagrams. The errors bars on the top right of each panel show the characteristic uncertainty in the emission line ratios.

ther $\log[\Sigma_{H\alpha}/(\text{erg s}^{-1} \text{ kpc}^{-2})] \leq 38.0$ or $\text{EW}(H\alpha) < 15 \text{ \AA}$, are denoted as DIG-dominated. Figure 6 displays our identified kpc-sized star forming regions on the B16 relation including the intrinsic dispersion in their data set, while Figure 7 shows the nebular emission line ratios compared to the Kewley et al. (2006) and Kauffmann et al. (2003) models in the standard BPT diagrams. The starburst-like, normal star forming, and DIG dominated regions are plotted in both Figures 6 and 7 for completeness. We note that there is no systematic trend with inclination, and almost all of our regions meet the $b/a > 0.42$ requirement described in Battisti et al. (2017). The measured flux densities in the *Swift* NUV

filters and the emission line flux from MaNGA are listed in Table 3, and the calculated properties for the 56 identified regions are listed in Table 4.

We tested the effects of aperture positioning and pixelation on the photometry by comparing two different error measurement methods: (1) we only include pixels whose center lies within the aperture, and (2) we calculate the exact boundary of the aperture within the pixel. We find the difference between these two methods was $\sim 2\%$ of the total error calculated for method (2), which is the most commonly adopted error calculation technique. Thus we find that the effects of aperture positioning and pixelation on the photometry is minimal, and we adopt method (2). Additionally, we find no systematic trends with β and signal-to-noise in either uvw1 or uvw2.

5.2 DIG-dominated regions

Of the 56 regions we identified, 14 are DIG-dominated according to the description above. For these regions, the $\langle \text{EW}(\text{H}\alpha) \rangle$ is about 17 \AA but they are “star forming” according to the BPT line ratios, and have a similar scatter in τ_B^l to the star forming and starburst-like regions. Kolmogorov-Smirnov (K-S) two-sample tests for each grouping of the three τ_B^l populations fail to show that the populations are statistically distinct, with p-values $0.59\text{--}0.79$. However, the DIG-dominated regions have systematically higher values of β ; K-S two-sample and Anderson-Darling tests (Stephens 1974) show distinct populations at the 95% significance level. The discrepant behavior in β and τ_B^l is likely because the UV light in the DIG-dominated regions is not dominated by massive stars, making β an unreliable tracer of the stellar continuum colour excess. As such, we exclude the DIG-dominated regions from future analysis.

5.3 Demographics of Star Forming Regions

Of the 42 remaining regions, 95% are defined as star forming and 5% as starburst-like. These regions have, larger $\langle \text{EW}(\text{H}\alpha) \rangle$ than the DIG-dominated regions, $\sim 58 \text{ \AA}$ for the star forming, and $\sim 130 \text{ \AA}$ for the starburst-like, and are quite similar to those from B16 ($\text{EW} \sim 40 \text{ \AA}$) and Calzetti et al. (1994, $\text{EW} \sim 110 \text{ \AA}$), respectively. These regions have physical areas that span a range of $4.7\text{--}67.1 \text{ kpc}^2$ with an average of 17.4 kpc^2 and a median of 13 kpc^2 . Most of the regions are truly kpc-sized, as 80% have areas less than 25 kpc^2 . B16 adopted a $4''5$ aperture and probed a similar redshift range so their regions are approximately the same size as those in our study.

Therefore this work builds on that of B16 by studying *resolved* regions across the faces of galaxies. We will begin by establishing consistency between the regions studied by B16 and those in this work, and employ statistical tests to characterize any dependence on the physical properties of both the resolved regions and the integrated galaxy light. Finally we will explore the dependence on aperture size by comparing the resolved regions to the integrated galaxy light, which was a test not possible in the B16 study.

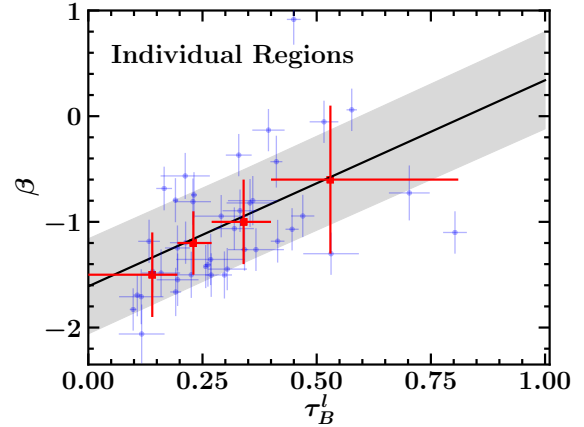


Figure 8. Same as Figure 6, but without the DIG-dominated regions (see discussion in Section 5.2.) The light blue circles are the measurements for the individual regions, and the red squares are the mean and associated sample dispersion for the binned data. The error bars on τ_B^l represent the size of the bin, while those on β represent the 1σ dispersion within the bin. All bins are statistically consistent with the B16 relation.

6 COMPARISON TO THE B16 MODEL

6.1 Intrinsic Scatter for Individual Regions

To examine the relationship between β and τ_B^l , we binned the data with respect to τ_B^l , and calculated the unweighted mean for β and τ_B^l , and the unweighted 1σ sample dispersion in β for each bin. The bins were defined to hold approximately equal numbers of data points and have a similar size to those used in B16. The results are reported in Table 5. The mean values and associated sample dispersions are plotted against the B16 relation in Figure 8. All four bins are statistically consistent with the B16 relation. The third bin is dominated by regions with $1.1 \leq D_n(4000) \leq 1.3$, whose importance will be described in Section 6.2. The bin with the highest τ_B^l values is sparsely populated. While more regions are needed to properly constrain the intrinsic scatter for $\tau_B^l > 0.4$, they are not easily detectable due to the high levels of extinction.

6.2 Stellar Age

As mentioned in Section 4.5, the value of $D_n(4000)$ is related to the relative contribution of the older and younger stellar populations, and is correlated with the measured slope between β and τ_B^l . Specifically, as the $D_n(4000)$ of the integrated light increases, so does the light from older stars. The result is a steeper slope as seen in Figure 20 of B16. We assessed this effect by using a combination of Bruzual & Charlot (2003, BC03) models. In order to simulate a star forming region with a strong contribution from an older stellar population, we created a multi-burst model by evolving the solar metallicity simple stellar population models. The first burst has an exponentially declining SFH with an e-folding time-scale of 700 Myr. The second burst also has an exponentially declining SFH, with a variable e-folding time-scale (700, 100 or 10 Myr). We separated the bursts by 10 Gyr and varied the relative mass ratio between the

Table 3. Flux Measurements of Star Forming Regions

Object I.D.	Region I.D.	Flux Densities ^a		Flux Measurements ^{b, c}						
		uvw2	uvw1	H β λ 4861	[O III] λ 5007	[O I] λ 6300	H α λ 6563	[N II] λ 6583	[S II] λ 6716	[S II] λ 6731
1	1.1	16 \pm 2	11 \pm 2	27 \pm 1	35 \pm 1	3 \pm 1	86 \pm 1	12 \pm 1	20 \pm 1	14 \pm 1
1	1.2	9 \pm 1	8 \pm 1	16 \pm 1	21 \pm 1	2 \pm 1	54 \pm 1	8 \pm 1	14 \pm 1	9 \pm 1
1	1.3	9 \pm 1	9 \pm 1	14 \pm 1	22 \pm 1	2 \pm 1	45 \pm 1	5 \pm 1	10 \pm 1	7 \pm 1
2	2.1	7.2 \pm 0.8	4.5 \pm 0.3	19 \pm 1	43 \pm 1	1 \pm 1	63 \pm 1	7 \pm 1	8 \pm 1	6 \pm 1
3	3.1	14.1 \pm 0.4	13.2 \pm 0.4	43 \pm 1	15 \pm 1	5 \pm 1	170 \pm 1	49 \pm 1	37 \pm 1	26 \pm 1
4	4.1	17.3 \pm 2.0	12 \pm 1	24 \pm 1	23 \pm 1	4 \pm 1	83 \pm 1	21 \pm 1	20 \pm 1	14 \pm 1
5	5.1	7.4 \pm 0.5	7.0 \pm 0.2	11 \pm 1	3 \pm 1	2 \pm 1	43 \pm 1	16 \pm 1	9 \pm 1	6 \pm 1
6	6.1	20 \pm 1	17 \pm 1	68 \pm 1	119 \pm 1	7 \pm 1	229 \pm 1	45 \pm 1	40 \pm 1	30 \pm 1
7	7.1	18.6 \pm 0.5	15.7 \pm 0.7	31 \pm 1	17 \pm 1	4 \pm 1	113 \pm 1	33 \pm 1	28 \pm 1	20 \pm 1
7	7.2	11.0 \pm 0.4	9.4 \pm 0.6	12 \pm 1	8 \pm 1	2 \pm 1	43 \pm 1	10 \pm 1	12 \pm 1	8 \pm 1
7	7.3	11.9 \pm 0.4	9.3 \pm 0.6	14 \pm 1	9 \pm 1	3 \pm 1	48 \pm 1	12 \pm 1	15 \pm 1	9 \pm 1
8	8.1	27 \pm 1	20.5 \pm 0.8	34 \pm 1	16 \pm 1	4 \pm 1	122 \pm 1	34 \pm 1	29 \pm 1	19 \pm 1
9	9.1	18.4 \pm 0.8	14.1 \pm 0.9	40 \pm 1	30 \pm 1	5 \pm 1	139 \pm 1	37 \pm 1	33 \pm 1	23 \pm 1
9	9.2	12.8 \pm 0.7	9.3 \pm 0.7	24 \pm 1	27 \pm 1	4 \pm 1	80 \pm 1	17 \pm 1	18 \pm 1	12 \pm 1
9	9.3	9.3 \pm 0.6	7.0 \pm 0.6	18 \pm 1	21 \pm 1	2 \pm 1	58 \pm 1	11 \pm 1	13 \pm 1	9 \pm 1
10	10.1	8.6 \pm 0.3	7.5 \pm 0.5	10 \pm 1	7 \pm 1	1 \pm 1	33 \pm 1	8 \pm 1	9 \pm 1	6 \pm 1
10	10.2	7.9 \pm 0.3	6.8 \pm 0.5	6 \pm 1	8 \pm 1	1 \pm 1	21 \pm 1	4 \pm 1	5 \pm 1	4 \pm 1
11	11.1	10.0 \pm 0.7	10.0 \pm 0.7	33 \pm 1	10 \pm 1	4 \pm 1	140 \pm 1	46 \pm 1	29 \pm 1	21 \pm 1
12	12.1	73 \pm 3	48 \pm 1	190 \pm 1	527 \pm 2	21 \pm 1	600 \pm 2	76 \pm 1	85 \pm 1	61 \pm 1
12	12.2	55 \pm 1	38 \pm 1	157 \pm 1	501 \pm 2	15 \pm 1	500 \pm 2	48 \pm 1	61 \pm 1	44 \pm 1
12	12.3	99 \pm 2	72 \pm 1	320 \pm 2	880 \pm 2	37 \pm 1	1054 \pm 2	152 \pm 1	156 \pm 1	114 \pm 1
13	13.1	79 \pm 5	67 \pm 5	275 \pm 2	413 \pm 2	19 \pm 1	952 \pm 2	193 \pm 1	153 \pm 1	109 \pm 1
13	13.2	63 \pm 4	43 \pm 4	129 \pm 1	145 \pm 1	14 \pm 1	447 \pm 2	118 \pm 1	88 \pm 1	63 \pm 1
13	13.3	47 \pm 4	40 \pm 4	261 \pm 2	737 \pm 2	22 \pm 1	941 \pm 2	136 \pm 1	123 \pm 1	89 \pm 1
14	14.1	7.9 \pm 0.3	10.1 \pm 0.7	93 \pm 1	74 \pm 1	12 \pm 1	418 \pm 2	126 \pm 1	62 \pm 1	54 \pm 1
15	15.1	122 \pm 3	93 \pm 2	227 \pm 2	131 \pm 2	20 \pm 1	913 \pm 2	285 \pm 2	174 \pm 2	122 \pm 2
16	16.1	9 \pm 1	8 \pm 1	14 \pm 1	5 \pm 1	3 \pm 1	56 \pm 1	21 \pm 1	11 \pm 1	8 \pm 1
16	16.2	10 \pm 2	7 \pm 1	17 \pm 1	5 \pm 1	2 \pm 1	65 \pm 1	22 \pm 1	13 \pm 1	10 \pm 1
17	17.1	29 \pm 2	27 \pm 1	110 \pm 1	26 \pm 1	11 \pm 1	476 \pm 2	204 \pm 1	80 \pm 1	65 \pm 1
18	18.1	6.8 \pm 0.5	5.9 \pm 0.7	26 \pm 1	11 \pm 1	6 \pm 1	151 \pm 1	60 \pm 1	33 \pm 1	23 \pm 1
19	19.1	26 \pm 1	21 \pm 1	97 \pm 1	25 \pm 1	9 \pm 1	433 \pm 2	214 \pm 1	69 \pm 1	58 \pm 1
20	20.1	21 \pm 3	15 \pm 2	26 \pm 1	7 \pm 1	3 \pm 1	103 \pm 1	33 \pm 1	20 \pm 1	13 \pm 1
20	20.2	16 \pm 3	14 \pm 2	23 \pm 1	4 \pm 1	3 \pm 1	85 \pm 1	30 \pm 1	18 \pm 1	12 \pm 1
20	20.3	11 \pm 2	9 \pm 2	18 \pm 1	5 \pm 1	2 \pm 1	70 \pm 1	24 \pm 1	13 \pm 1	11 \pm 1
21	21.1	16 \pm 2	13 \pm 1	18 \pm 1	4 \pm 1	1 \pm 1	80 \pm 1	27 \pm 1	9 \pm 1	7 \pm 1
22	22.1	48 \pm 3	37 \pm 2	95 \pm 1	31 \pm 1	10 \pm 1	412 \pm 2	160 \pm 1	76 \pm 1	56 \pm 1
23	23.1	13.0 \pm 0.7	13.3 \pm 0.4	23 \pm 1	6 \pm 1	2 \pm 1	98 \pm 1	38 \pm 1	16 \pm 1	11 \pm 1
23	23.2	13.6 \pm 0.7	11.9 \pm 0.4	17 \pm 1	4 \pm 1	2 \pm 1	70 \pm 1	28 \pm 1	13 \pm 1	9 \pm 1
23	23.3	10.0 \pm 0.6	8.9 \pm 0.3	20 \pm 1	9 \pm 1	2 \pm 1	69 \pm 1	24 \pm 1	15 \pm 1	10 \pm 1
23	23.4	29 \pm 1	22.5 \pm 0.5	52 \pm 1	41 \pm 1	4 \pm 1	168 \pm 1	52 \pm 1	31 \pm 1	22 \pm 1
24	24.1	8.2 \pm 0.5	7.0 \pm 0.3	20 \pm 1	6 \pm 1	2 \pm 1	80 \pm 1	28 \pm 1	13 \pm 1	10 \pm 1
24	24.2	10.3 \pm 0.6	8.7 \pm 0.3	22 \pm 1	5 \pm 1	2 \pm 1	88 \pm 1	31 \pm 1	15 \pm 1	10 \pm 1
25	25.1	11.9 \pm 0.3	9.0 \pm 0.3	18 \pm 1	5 \pm 1	2 \pm 1	74 \pm 1	22 \pm 1	15 \pm 1	10 \pm 1
25	25.2	20.3 \pm 0.4	16.0 \pm 0.4	61 \pm 2	31 \pm 1	7 \pm 1	390 \pm 2	117 \pm 1	54 \pm 1	43 \pm 1
25	25.3	19.1 \pm 0.4	15.6 \pm 0.4	50 \pm 1	9 \pm 1	5 \pm 1	228 \pm 1	71 \pm 1	35 \pm 1	24 \pm 1
25	25.4	21.8 \pm 0.4	22.1 \pm 0.4	41 \pm 1	8 \pm 1	5 \pm 1	198 \pm 1	61 \pm 1	25 \pm 1	18 \pm 1
25	25.5	9.6 \pm 0.3	8.0 \pm 0.3	30 \pm 1	9 \pm 1	3 \pm 1	120 \pm 1	36 \pm 1	22 \pm 1	16 \pm 1
25	25.6	16.1 \pm 0.4	12.8 \pm 0.3	27 \pm 1	7 \pm 1	3 \pm 1	108 \pm 1	34 \pm 1	17 \pm 1	14 \pm 1
26	26.1	32.7 \pm 0.5	23 \pm 1	66 \pm 3	46 \pm 1	9 \pm 1	236 \pm 1	72 \pm 1	48 \pm 1	35 \pm 1
26	26.2	133 \pm 1	97 \pm 2	509 \pm 2	497 \pm 2	38 \pm 1	1883 \pm 2	478 \pm 2	268 \pm 1	198 \pm 1
26	26.3	78.9 \pm 0.8	58 \pm 1	266 \pm 2	244 \pm 1	22 \pm 1	989 \pm 2	259 \pm 1	159 \pm 1	110 \pm 1
26	26.4	90 \pm 1	65 \pm 1	115 \pm 1	61 \pm 1	10 \pm 1	429 \pm 2	133 \pm 1	83 \pm 1	57 \pm 1
26	26.5	27.2 \pm 0.5	19.5 \pm 0.8	81 \pm 1	53 \pm 1	9 \pm 1	310 \pm 2	92 \pm 1	53 \pm 1	37 \pm 1
27	27.1	3.0 \pm 0.2	2.8 \pm 0.2	6 \pm 1	1 \pm 1	1 \pm 1	24 \pm 1	11 \pm 1	5 \pm 1	4 \pm 1
28	28.1	40 \pm 1	42 \pm 2	148 \pm 2	39 \pm 2	16 \pm 1	755 \pm 2	263 \pm 2	105 \pm 2	72 \pm 2
29	29.1	15.8 \pm 0.7	12.0 \pm 0.6	13 \pm 1	7 \pm 1	2 \pm 1	63 \pm 1	26 \pm 1	7 \pm 1	6 \pm 1

^a Flux densities for the Swift uvw1 and uvw2 filters are presented in units of 10^{-17} erg s $^{-1}$ cm $^{-2}$ Å $^{-1}$ and without a K-correction, but are corrected for foreground extinction. See Section 4.2.3 for details.

^b Fluxes for emission lines are presented in units of 10^{-17} erg s $^{-1}$ cm $^{-2}$ and are corrected for foreground extinction. See Section 4.2.1 for details.

^c The systematic uncertainty in emission line flux as described by Belfiore et al. (2019) is included in the reported error. See Section 3.1 for details.

Table 4. Derived Quantities of Star Forming Regions

Region I.D.	Dist. ^a (kpc)	Area (kpc ²)	$\log(\Sigma_{\text{H}\alpha}/[\text{erg s}^{-1} \text{ kpc}^{-2}])^b$	β	τ_B^l ^b	$12 + \log([\text{O}/\text{H}])^{b,c}$	$D_n(4000)^d$	EW(H α) ^b (Å)
1.1	2.6	4.7	38.024±0.006	−1.7±0.3	0.12±0.05	8.6±0.3	1.26±0.06	32±2
1.2	0.1	4.7	37.968±0.008	−0.6±0.2	0.16±0.07	8.7±0.3	1.31±0.04	23±1
1.3	1.9	4.1	37.89±0.01	−0.1±0.2	0.10±0.07	8.6±0.3	1.23±0.06	40±3
2.1	4.3	13.4	38.249±0.007	−2.1±0.3	0.12±0.05	8.5±0.3	1.14±0.08	101±5
3.1	0.2	21.5	38.454±0.003	−0.4±0.2	0.33±0.03	9.0±0.3	1.22±0.04	41±2
4.1	0.9	20.2	38.247±0.006	−1.5±0.2	0.20±0.05	8.9±0.3	1.33±0.04	21±1
5.1	0.5	4.1	38.12±0.01	−0.3±0.3	0.4±0.1	9.0±0.3	1.44±0.04	8.4±0.8
6.1	1.3	19.7	38.753±0.003	−0.7±0.2	0.17±0.02	8.7±0.3	1.26±0.02	33±1
7.1	0.3	10.7	38.254±0.005	−0.8±0.2	0.23±0.04	8.9±0.3	1.33±0.04	19.0±0.8
7.2	3.9	9.4	37.83±0.01	−0.8±0.2	0.26±0.09	8.8±0.3	1.26±0.04	20±1
7.3	4.1	10.8	37.88±0.01	−1.1±0.2	0.17±0.08	8.9±0.3	1.28±0.04	17±1
8.1	0.5	15.7	38.517±0.004	−1.2±0.2	0.21±0.03	8.9±0.3	1.23±0.04	32±1
9.1	1.8	33.8	38.286±0.004	−1.2±0.2	0.20±0.03	8.8±0.3	1.25±0.02	28±1
9.2	5.6	34.0	38.046±0.007	−1.5±0.2	0.16±0.04	8.7±0.3	1.24±0.04	35±2
9.3	8.7	34.0	37.903±0.008	−1.3±0.2	0.13±0.05	8.7±0.3	1.21±0.04	37±2
10.1	0.9	21.8	37.807±0.01	−0.7±0.2	0.1±0.1	8.8±0.3	1.29±0.04	11±1
10.2	3.3	17.5	37.61±0.02	−0.8±0.2	0.1±0.1	8.7±0.3	1.2±0.1	15±2
11.1	0.2	22.0	38.420±0.004	−0.1±0.2	0.39±0.04	9.0±0.3	1.32±0.04	28±1
12.1	2.2	25.3	39.186±0.001	−1.8±0.2	0.098 ± 0.008	8.5±0.3	1.00±0.02	185±2
12.2	4.8	25.3	39.011±0.001	−1.7±0.2	0.107±0.009	8.4±0.3	1.02±0.02	149±2
12.3	1.7	25.3	39.335±0.001	−1.5±0.2	0.141±0.005	8.5±0.3	1.04±0.02	142±1
13.1	2.9	5.8	39.298±0.001	−0.8±0.2	0.191±0.006	8.7±0.3	1.08±0.02	155±2
13.2	0.3	5.8	38.971±0.002	−1.7±0.2	0.19±0.01	8.8±0.3	1.21±0.02	49±1
13.3	2.8	7.6	39.296±0.001	−0.7±0.2	0.231±0.007	8.5±0.3	1.02±0.02	236±3
14.1	0.6	15.3	39.064±0.002	0.9±0.2	0.45±0.02	8.8±0.3	1.37±0.04	50±1
15.1	0.3	8.9	39.206±0.001	−1.3±0.2	0.342±0.008	8.9±0.3	1.18±0.02	47±1
16.1	1.1	13.0	37.855±0.002	−0.5±0.2	0.36±0.09	9.0±0.3	1.50±0.06	8.1±0.8
16.2	4.6	8.2	37.99±0.01	−1.4±0.2	0.27±0.08	9.0±0.3	1.39±0.08	17±2
17.1	0.3	5.8	39.068±0.009	−0.4±0.2	0.41±0.01	9.1±0.3	1.32±0.02	35±1
18.1	0.9	16.2	38.222±0.002	−0.7±0.3	0.70±0.04	9.0±0.3	1.45±0.04	19.4±0.8
19.1	0.9	29.9	38.939±0.004	−1.1±0.2	0.45±0.01	9.1±0.3	1.24±0.02	43±1
20.1	1.0	8.4	38.452±0.002	−1.4±0.2	0.30±0.04	9.0±0.3	1.27±0.04	28±1
20.2	0.7	8.4	38.370±0.005	−0.8±0.2	0.27±0.05	9.1±0.3	1.35±0.02	14.2±0.8
20.3	1.2	8.3	38.381±0.006	−0.9±0.2	0.29±0.06	9.0±0.3	1.29±0.04	23±2
21.1	0.5	11.0	38.840±0.007	−0.9±0.2	0.44±0.07	9.1±0.3	1.54±0.04	7.5±0.5
22.1	1.4	39.0	38.260±0.002	−1.2±0.2	0.41±0.01	9.0±0.3	1.21±0.02	40±1
23.1	0.7	14.2	38.260±0.006	0.0±0.2	0.38±0.05	9.1±0.3	1.47±0.02	9.1±0.4
23.2	2.3	14.2	38.115±0.007	−0.7±0.2	0.34±0.06	9.1±0.3	1.41±0.04	11.1±0.6
23.3	5.1	14.2	38.109±0.007	−0.6±0.2	0.21±0.05	8.9±0.3	1.30±0.02	26±2
23.4	5.4	14.2	38.496±0.003	−1.2±0.2	0.13±0.02	8.8±0.3	1.15±0.02	44±2
24.1	5.5	23.1	38.386±0.007	−0.8±0.2	0.36±0.05	9.0±0.3	1.27±0.06	26±2
24.2	3.7	23.3	38.427±0.006	−0.8±0.2	0.35±0.05	9.1±0.3	1.27±0.06	27±2
25.1	4.4	8.2	38.253±0.007	−1.3±0.2	0.37±0.06	9.0±0.3	1.22±0.04	38±2
25.2	6.4	8.2	39.984±0.002	−1.1±0.2	0.80±0.03	8.9±0.3	1.21±0.04	113±2
25.3	3.4	11.9	39.747±0.003	−0.9±0.2	0.47±0.03	9.1±0.3	1.27±0.02	36±1
25.4	0.7	8.2	39.683±0.003	−0.1±0.2	0.52±0.03	9.1±0.3	1.37±0.02	16±1
25.5	5.8	8.1	38.464±0.004	−0.9±0.2	0.33±0.04	9.0±0.3	1.25±0.04	40±2
25.6	6.1	8.2	38.419±0.005	−1.1±0.2	0.32±0.04	9.0±0.3	1.21±0.04	39±2
26.1	6.4	9.8	38.847±0.003	−1.5±0.2	0.23±0.05	8.9±0.3	1.19±0.02	46±2
26.2	4.9	9.5	39.748±0.001	−1.4±0.2	0.257±0.004	8.8±0.3	1.05±0.02	217±2
26.3	6.3	12.7	39.469±0.001	−1.4±0.2	0.262±0.006	8.8±0.3	1.08±0.02	152±2
26.4	7.8	9.5	39.110±0.002	−1.5±0.2	0.27±0.01	8.9±0.3	1.12±0.02	54±1
26.5	8.0	9.5	38.965±0.002	−1.5±0.2	0.30±0.02	8.9±0.3	1.19±0.02	78±2
27.1	9.0	65.8	37.53±0.02	−0.3±0.2	0.4±0.1	9.1±0.3	1.50±0.08	11±1
28.1	1.2	56.3	39.243±0.001	0.1±0.2	0.58±0.01	9.1±0.3	1.28±0.02	37±1
29.1	1.3	67.1	38.286±0.006	−1.3±0.2	0.53±0.06	9.0±0.3	1.38±0.02	15.4±0.4

^a Distance is the difference between the nuclear coordinate of the galaxy from Table 2 and the centre of the region’s aperture.^b The systematic uncertainty in emission line flux as described by Belfiore et al. (2019) is included in the reported error. See Section 3.1 for details.^c Metallicity is calculated using the $([\text{O III}]/\text{H}\beta)/([\text{N II}]/\text{H}\alpha)$ ratio as described in as described in Pettini & Pagel (2004), and converted to Tremonti et al. (2004) via Kewley & Ellison (2008). The error bar includes the 0.3 dex uncertainty in the Pettini & Pagel (2004) relation, which is the largest uncertainty associated with the measurement. See Section 6.3 for details.^d The systematic uncertainty in $D_n(4000)$ as described by Westfall et al. (2019) is included in the reported error. See Section 3.1 for details.

Table 5. Values for τ_B^l bins

Bin Size	N ^a	$\langle\tau_B^l\rangle^b$	$\langle\beta\rangle^b$	$\sigma(\beta)^c$
$0.0 \leq \tau_B^l < 0.195$	10	0.14	-1.5	0.4
$0.195 \leq \tau_B^l < 0.27$	11	0.23	-1.2	0.3
$0.27 \leq \tau_B^l < 0.4$	11	0.34	-1.0	0.4
$0.4 \leq \tau_B^l < 0.81$	10	0.53	-0.6	0.7

^a N is the number of regions within the τ_B^l bin.

^b The reported values are the means of τ_B^l and β in each bin.

^c $\sigma(\beta)$ is the 1σ dispersion of the β values in each bin.

older and younger populations from 1:1 to 100:1. We show the results at $t = 100$ Myr after the second burst for each of the three described SFHs in Figure 9. The intrinsic β in each case increases by ~ 0.03 between these two older to younger mass ratios; this is much smaller than the 1σ sample dispersion in β . However, the initial β and $D_n(4000)$ are strongly tied to the current SFR and SFH, as clearly demonstrated by Figure 9 (see Section 4.4 for a discussion of the assumed intrinsic β). This result corroborates the minimal effects of the older stellar population on the β - τ_B^l for $D_n(4000) \lesssim 1.5$ presented in B16.

In addition to $D_n(4000)$, we measured the $\text{EW}(\text{H}\alpha)$ for all the identified kpc-sized regions, a proxy for the specific SFR (sSFR), as well as an indicator of the contribution from the older stellar population. All of the identified regions have $\text{EW}(\text{H}\alpha) > 15$ Å, a value 2.5 times larger than that used to classify kpc-sized regions as star forming (Sánchez et al. 2014; Wang et al. 2018). We will therefore assume for the rest of the paper that the measured β values are not significantly affected by UV light from the older stellar population.

The individual regions exhibit a trend with stellar age similar to that found by B16, as shown in Figure 10. The B16 relation is displayed, as well as the least squares linear fits to our data for the regions with $D_n(4000) > 1.3$ and $1.1 \leq D_n(4000) \leq 1.3$. The latter corresponds to the values used for the B16 relation, and, within the errors, are well fitted by the slope and intercept derived by B16.

Regions with larger $D_n(4000)$ measurements require a steeper slope and higher intercept than that of B16. A K-S two-sample test comparing β for the two $D_n(4000)$ bins shows that the distributions are statistically distinct at the 99% confidence interval. The physical environment may be different for young, dusty systems, but we lack sufficient data in the low $D_n(4000)$ bin to provide any quantitative explanation for their behavior. We conclude that the B16 law is only applicable to regions with a measured $D_n(4000)$ between 1.1 and 1.3. Finally, we see no significant trends with $\text{EW}(\text{H}\alpha)$, confirming that our $\Sigma_{\text{H}\alpha}$ and $\text{EW}(\text{H}\alpha)$ criteria are robust indicators of star forming regions.

6.3 Dependence of β and τ_B^l on Metallicity and SFR

In addition to deriving the β - τ_B^l relation, B16 fitted second order polynomials to the β and τ_B^l measurements with respect to different physical properties, including metallicity, SFR and Σ_{SFR} . We compare the measured properties for the regions in our sample to those fitted relations

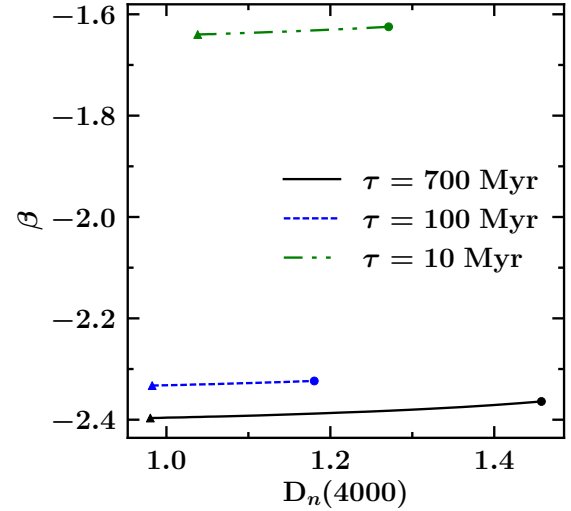


Figure 9. β vs. $D_n(4000)$ for the simulated multi-burst models described in Section 6.2. In each case the old population is modeled with an exponentially decaying SFH and an e-folding time-scale of 700 Myr. This is combined with a younger burst with an exponentially decaying SFH and an e-folding time of either 700 Myr (black solid line), 100 Myr (blue dashed line) or 10 Myr (green dot-dashed line). The second burst is placed 10 Gyr after the first burst, and is computed with different mass ratios of the older to younger populations, ranging from 1:1 (filled triangle) to 100:1 (filled circle). We plot the values for β and $D_n(4000)$ 100 Myr after the second burst. The effect of the older stellar population on β is minimal compared to the assumed SFH. Given the strong $\text{H}\alpha$ detections, implying recent star formation, we assume β is a robust tracer of the stellar continuum attenuation.

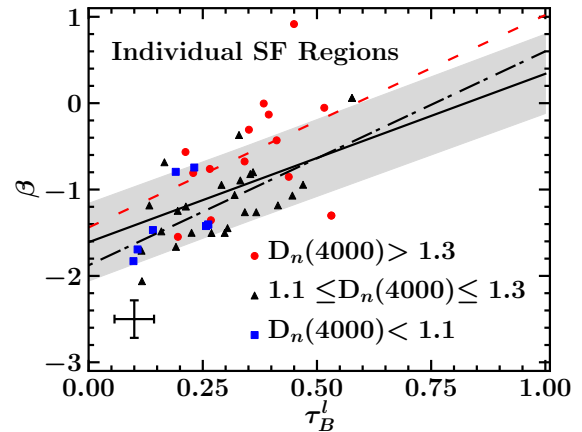


Figure 10. Same as Figure 8, but colour coded according to the measured $D_n(4000)$. The red circles represent regions with $D_n(4000) > 1.3$, black triangles with $1.1 \leq D_n(4000) \leq 1.3$, and blue squares with $D_n(4000) < 1.1$. The B16 relation was fit only to galaxies with measured $1.1 \leq D_n(4000) \leq 1.3$. The black dot-dashed line represents the fit to the regions in this work with the same $D_n(4000)$ constraints as B16, and the fits are very similar. The red dashed line is the fit to the regions in this work with $D_n(4000) > 1.3$. The fit to the older population has a higher intercept and steeper slope than that of B16. We do not attempt to fit the regions with $D_n(4000) < 1.1$ because of the small number of such regions.

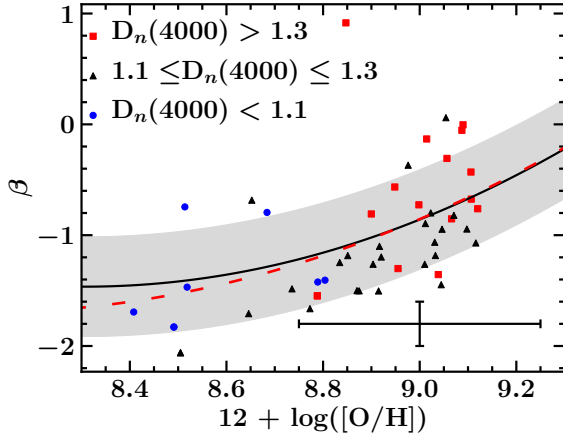


Figure 11. The measured β vs. metallicity for individual star forming regions. The solid line and gray shaded region are the fitted model and scatter from B16. The red dashed line is the fit to the data from this work. The metallicity is converted from the Pettini & Pagel (2004) system to that of Tremonti et al. (2004) for consistency. The uncertainty in the metallicity conversion and β are indicated by the error bar in the bottom right. We approximately recover the B16 relation.

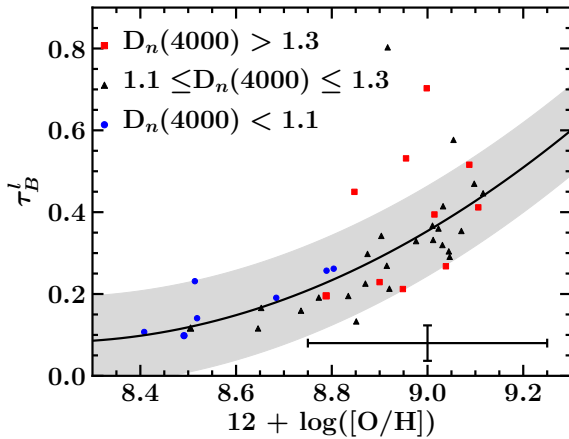


Figure 12. Same as Figure 11, but for τ_B^l . The data agree well with the model for $\tau_B^l \lesssim 0.5$.

given by B16. In order to have a fair comparison, we calculated metallicities for our star forming regions using the $([\text{O III}]/\text{H}\beta)/([\text{N II}]/\text{H}\alpha)$ ratio as described in Pettini & Pagel (2004), and converted to the Tremonti et al. (2004) system via the prescription of Kewley & Ellison (2008). The SFR and Σ_{SFR} values were measured using the $\text{H}\alpha$ luminosity as described in Kennicutt & Evans (2012). The SFR used in B16 came from Brinchmann et al. (2004), who also used $\text{H}\alpha$ to estimate a global SFR for SDSS galaxies.

Figures 11 and 12 compare the measured metallicities to the fitted B16 relations for β and τ_B^l . We note that unlike the β - τ_B^l relation, the metallicity, SFR, and Σ_{SFR} fits presented in B16 include *all* regions regardless of their $D_n(4000)$ measurement. We fitted a second order polynomial to the β -metallicity relation and include all data, regardless of the $D_n(4000)$ measurement, as shown in Figure 11. The resulting fit for β is almost identical to that of B16, albeit with a larger

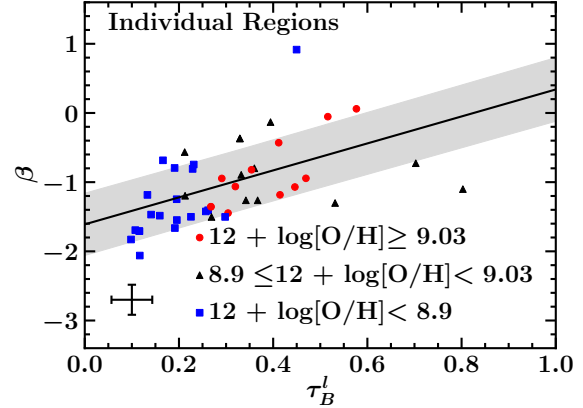


Figure 13. Same as Figure 10, but colour coded according to the metallicity for the individual regions. The metallicity is converted from the Pettini & Pagel (2004) system to that of Tremonti et al. (2004) for consistency. The B16 relation describes the data regardless of metallicity.

intrinsic scatter (0.51 in β). The regions with $D_n(4000) > 1.3$ have higher metallicity and drive the overall fit. We conclude that, unlike the β - τ_B^l relation, the relation between nebular metallicity and β seen in B16 is strongly influenced by the regions with $D_n(4000) > 1.3$.

Our data are also consistent with the τ_B^l -metallicity relation from B16 for $\tau_B^l \lesssim 0.5$. Above that threshold the measured metallicity underestimates τ_B^l . It is unclear whether this behavior is due to the inability of the B16 model to predict high values of τ_B^l or due to systematic errors when converting the metallicities. However, caution should be used when applying this model for high τ_B^l systems. Overall, metallicity, as estimated from the strong lines of $[\text{O III}]$ and $[\text{N II}]$, appears to be a valid indicator for both β and τ_B^l in low dust-content star forming regions, regardless of the $D_n(4000)$ measurement.

Unfortunately, these relations between dust content and metallicity are subject to strong systematic effects, such as the viewing angle or total gas column density, which can vary independent of metallicity. Thus we also looked at the scatter of the individual regions about the β - τ_B^l relation with respect to metallicity, as shown in Figure 13. The B16 law adequately describes the data regardless of metallicity. This lack of dependence on metallicity is consistent with the findings of Salim et al. (2018).

B16 also found relations similar to those of Figures 11 and 12, but for SFR and Σ_{SFR} . We looked for the same relations in our star forming regions, using the SFR calculated from the $\text{H}\alpha$ emission line and the relation given in Kennicutt & Evans (2012). We find very poor agreement between the properties of our individual star forming regions and the β -SFR, τ_B^l -SFR, β - Σ_{SFR} and τ_B^l - Σ_{SFR} relations described in B16. We conclude that these physical properties are not useful in constraining either β or τ_B^l .

6.4 Distance from Galaxy Centre

To test whether galactocentric radius plays a role in the β - τ_B^l relation, we calculated the distance between each galaxy's nucleus, as given by the MaNGA collaboration, and the cen-

tre of the apertures used to measure its star forming regions. The majority of the older regions, as probed by $D_n(4000)$, are near the nucleus as expected; however, we see no statistically significant change between the measured β , τ_B^l or metallicity between nuclear (within ~ 2 kpc of galaxy centre) and off-nuclear regions at the 95% confidence level. The marginal p-value for τ_B^l , 0.09, is most likely due to the difference in total dust content, which falls exponentially with distance from the nucleus (Peletier et al. 1995; Giovanelli et al. 1994). Therefore, any change seen in the β – τ_B^l relation with distance from galaxy centre is most likely a direct consequence of the change in total dust content, and is not statistically significant.

7 DEPENDENCE OF LOCAL ATTENUATION ON GALAXY-SCALE AND LOCAL PROPERTIES

7.1 Dependence on Large-Scale Properties

The total dust content, metallicity, and SFR all scale with galaxy mass, and all are associated with changes in the intrinsic attenuation curve (e.g., Tremonti et al. 2004; Calzetti et al. 2000; Calzetti 2001; Wild et al. 2011; Xiao et al. 2012; Salim et al. 2018). Any scatter between the kpc-sized regions and the B16 model could therefore be the result of the different physical environments present within the galaxies in our sample. To test this hypothesis, we examined the effect of the *integrated galaxy* stellar mass and SFR on the β – τ_B^l relation for the *individual* star forming regions. Here we define the “integrated” emission as that within the IFU footprint on the galaxy, as described in Section 4.2.1, which may not perfectly represent the global galaxy value. We also compare the β and τ_B^l measurements between the integrated galaxy light and individual star forming regions in Section 7.2.

7.1.1 Stellar Mass

Salim et al. (2018) concluded that the UV slope of the attenuation curve for the integrated light steepens in lower-mass galaxies, which they associate with a lower dust content. A similar trend with stellar mass (or metallicity, as the two properties are related; see Tremonti et al. 2004) is present in our β – τ_B^l measurements for the integrated galaxy light (see Figure 14). Given our small sample size, we separate our objects into two mass bins, those above and below $\log(M_*/M_\odot) = 9.6$; this definition is roughly consistent with the commonly used division between dwarf and high mass galaxies ($\log[M_*/M_\odot] \sim 9.5$). The observed trend in our data persists when galaxies with high inclination angles ($b/a < 0.42$) are excluded (i.e., those where the UV bump might be present; see Battisti et al. 2017, for details), and is not due to systematic changes in $D_n(4000)$ or $\Sigma_{H\alpha}$.

The individual regions from the galaxies sorted by the mass of the parent galaxy are compared to the β – τ_B^l relation from B16 in Figure 15. After excluding the region with $\beta \approx 1$, the slope between β and τ_B^l for the individual regions in low-mass galaxies is only slightly shallower than that for the parent galaxy. This result is likely driven by the fact that the individual regions in low-mass galaxies have preferentially lower τ_B^l values; the K-S two sample test for

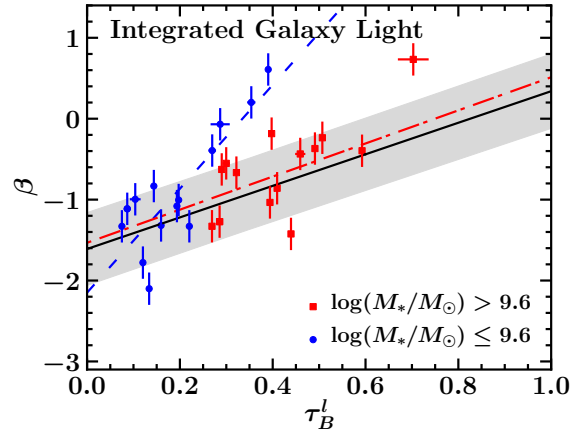


Figure 14. The β vs. τ_B^l measurements from the integrated galaxy light of the objects in our sample, colour-coded according to the stellar mass of the galaxy. The solid black line and gray shaded region are the B16 relation and sample dispersion, respectively. The blue dashed line is the least squares linear fit to the galaxies to the lowest stellar mass bin [$\log(M_*/M_\odot) \lesssim 9.6$] in this sample. The red dot-dashed line is the fit to the galaxies in the high stellar mass bin. The lowest mass bin has a significantly steeper slope than that measured for the high mass bin.

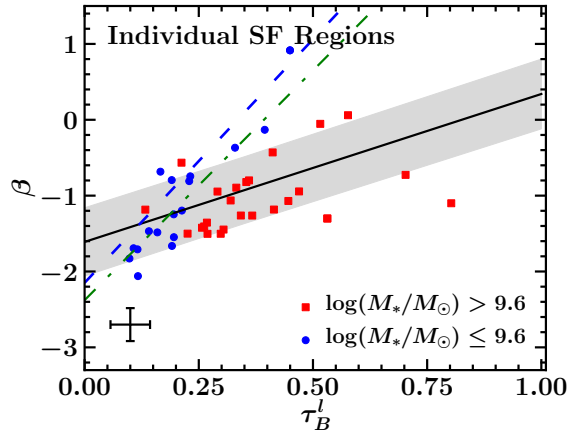


Figure 15. β vs. τ_B^l measurements from the individual star forming regions colour-coded according to the stellar mass of the parent galaxy. The solid black line and gray shaded region are the B16 relation and sample dispersion, respectively. The blue dashed line is the fit to the integrated light of low-mass galaxies, as shown in Figure 14. The green dot-dashed line is the least squares fit to the individual regions of low-mass galaxies *excluding* the one outlier at $\beta \approx 1$. The error bar on the lower left represents the characteristic uncertainty in β and τ_B^l .

τ_B^l shows evidence of distinctly different distributions at the 99% confidence level, while that of β does not. We additionally see no systematic trends with $D_n(4000)$ or $\Sigma_{H\alpha}$ between the two mass bins, similar to that of the integrated galaxy light.

There are three possible methodological explanations for our result: 1) our $\Sigma_{H\alpha}$ and $\text{EW}(H\alpha)$ cuts are not sufficient to eliminate all regions that are dominated by DIG, 2) our assumption that the 2175 Å bump is absent is not valid, and must be included in our estimate of the relation between

β and τ_B^l , or 3) the $D_n(4000)$ or $EW(H\alpha)$ are systematically different in low-mass galaxies hence the slope described by B16 is not appropriate. As shown in Table 4, the $\Sigma_{H\alpha}$ values of the individual regions from low-mass galaxies span the range $\log[\Sigma_{H\alpha}/(M_\odot \text{ yr}^{-1} \text{ kpc}^{-2})] = 38.05\text{--}39.3$, while those from the high-mass galaxies extend to slightly higher surface brightnesses, $\log[\Sigma_{H\alpha}/(M_\odot \text{ yr}^{-1} \text{ kpc}^{-2})] = 38.06\text{--}39.7$. Similarly, for low-mass galaxies, the median $D_n(4000) = 1.234$ is not dissimilar to the value from higher-mass galaxies, 1.247. While the average $H\alpha$ equivalent width is higher for the regions from low-mass galaxies (78 Å) than that for high-mass galaxies (50 Å), neither indicate a very low sSFR. Thus, it is unlikely that either the $\Sigma_{H\alpha}$ cut or dilution from the older stellar population are the main causes of the observed steeper slope.

Therefore, the only methodological issue that could explain this discrepancy is the 2175 Å bump, which we are neglecting in this analysis. If the bump strength was similar to that of the Milky Way, the values of β calculated in this work would be overestimated. Moreover, the 2175 Å bump is more prominent in lower-mass star forming galaxies and quiescent galaxies. However, Battisti et al. (2017) found that the bump is only significant in star forming galaxies when $b/a < 0.42$. Also, the UVOT filters we are using in our analysis are broad: the uvw2 filter, which includes the 2175 Å feature, is almost five times wider than the feature itself, thus diluting any effect this absorption feature might have. Finally, the trend is not dependent on any regions with galaxies with high inclination angles, implying that this is not caused by the 2175 Å bump.

Thus we cannot find any strong systematic issues that could cause this dependence of $\beta\text{--}\tau_B^l$ on stellar mass. This exact trend is also seen in Salim et al. (2018), which they interpret to be a result of higher A_V values in more massive galaxies. Future studies should include kiloparsec-sized regions both from starburst galaxies (which have a higher dust content due to the high SFR), and star forming galaxies spanning a wide range of stellar mass to disentangle this issue. Both of these requirements can easily be met by increasing the current overlap between *Swift* and MaNGA galaxies.

7.1.2 Star Formation Rate

The total SFR of a galaxy affects the slope between the integrated values of β and τ_B^l . This connection is evident when comparing the results of Calzetti et al. (1994) and B16. The individual regions show a bias to lower β values when the integrated SFR is above $\log[\text{SFR}_{1R_e}[H\alpha]/(M_\odot \text{ yr}^{-1})] > 0$. A K-S 2 sample test for the β measurements between the regions in the highest integrated SFR bin and the other two bins reveal that they are statistically distinct at the 90% confidence level. However, all of the regions in the high integrated SFR bin reside in a total of six galaxies (Table 2), all with $\log[\text{SFR}_{1R_e}[H\alpha]/(M_\odot \text{ yr}^{-1})] < 1$. In order to fully constrain this potential effect, we need a larger sample of high star formation rate galaxies.

7.2 Comparing Local and Global Measures of β and τ_B^l

The integrated flux from galaxies includes emission from star forming regions, DIG, the underlying older stellar popula-

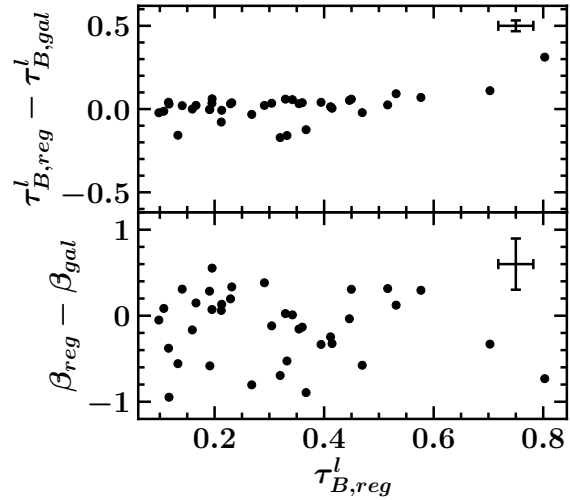


Figure 16. The difference between the measured τ_B^l (top panel) and β (lower panel) values from the individual region and those derived from the integrated galaxy light as a function of the measured τ_B^l from the individual regions. The ordinates span the same range of total attenuation, given the B16 relation of $\beta = 1.95\tau_B^l - 1.61$. β shows significant local variation, while τ_B^l is remarkably consistent between the two scales. The error bar in the upper right corner in each panel shows the characteristic uncertainty associated with these measurements.

tion, and all other sources of light. The kpc-sized star forming regions should have a relatively larger contribution from the younger stellar populations, albeit with some contamination from DIG (see Section 5). As a result, β and τ_B^l do not necessarily need to match between the two very different spatial scales. Figures 16 and 17 make this comparison using the measured τ_B^l and β from the individual star forming regions and from the galaxy as a whole. The ordinates in the two panels have been scaled to represent the same amount of attenuation given the B16 relation. The dichotomy is striking: while τ_B^l for the individual regions largely agrees with that for the integrated galaxy light, β values exhibit a large amount of scatter. We also note a trend at high levels of nebular attenuation where the values of β from the individual regions are smaller than that for the integrated galaxy value and vice versa for τ_B^l .

Given the scaling effects between the optical nebular and UV stellar continuum attenuation, we present in Figure 18 the fractional difference $\Delta\beta$ between the observed values and the predicted value, using $\Delta\tau_B^l$ and the B16 relation, $\beta = 1.95\tau_B^l - 1.61$. Clearly, β varies drastically between the two aperture sizes while τ_B^l remains within $\sim 50\%$ of the integrated galaxy value. The variation of β due to aperture size is also larger than the intrinsic scatter of $\sigma_{\text{int}} = 0.44$ seen in B16. We attempted to quantify the observed trends in τ_B^l and β by searching for any dependence on distance from the nucleus, $D_n(4000)$, metallicity and other parameters, as described below.

7.2.1 Distance from Nucleus

The difference between τ_B^l for the individual regions and for the integrated galaxy value is negatively correlated with

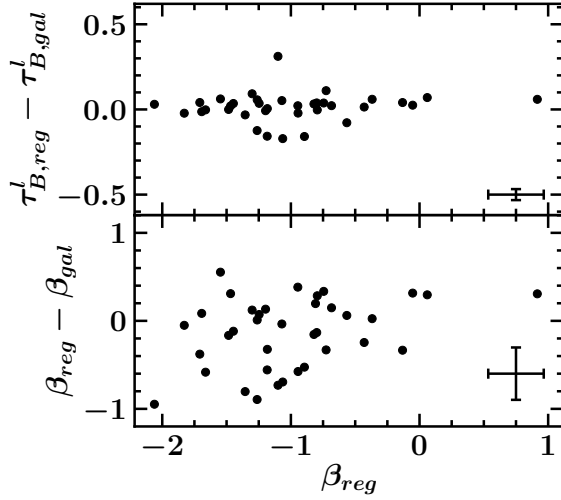


Figure 17. Same as Figure 16, but as a function of β from the individual regions. The error bar in the lower left corner in each panel shows the characteristic uncertainty for these measurements.

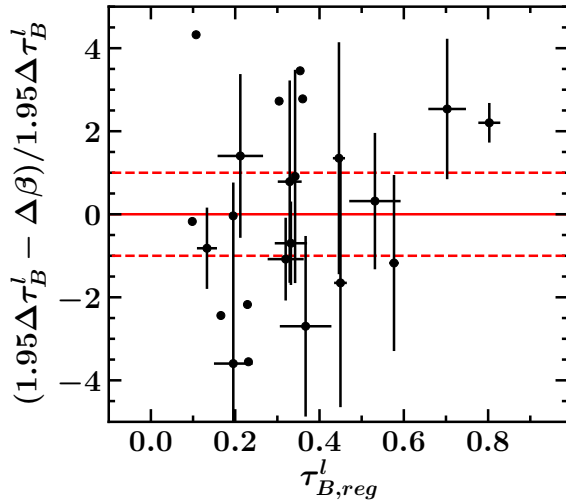


Figure 18. The fractional difference between the measured difference in $\Delta\beta$ to that predicted by B16 from $\Delta\tau_B^l$ as described in Figure 16. The solid red line denotes perfect agreement with the model, while the dashed red lines represent a departure of 100% from the expected value. The scatter between the optical and UV attenuation is significant even after including scaling differences. The uncertainties for measurements with $\Delta\tau_B^l < 0.05$ are not shown for clarity; while all of the values are well-measured, the small $\Delta\tau_B^l$ values create large errors when propagated.

distance from the nucleus. This behavior is illustrated in Figure 19. The Spearman and Kendall nonparametric correlation tests (Spearman 1904; Kendall 1938) show the two parameters are correlated at the 99% confidence level. We fitted the data with a second order polynomial, which produced the relation

$$\Delta\tau_B^l = -0.00637d^2 + 0.01418d + 0.0328, \quad (3)$$

where d is the distance from the nucleus in kiloparsec; the intrinsic dispersion is $\sigma_{\text{int}} = 0.08$. The one outlier seen at a dis-

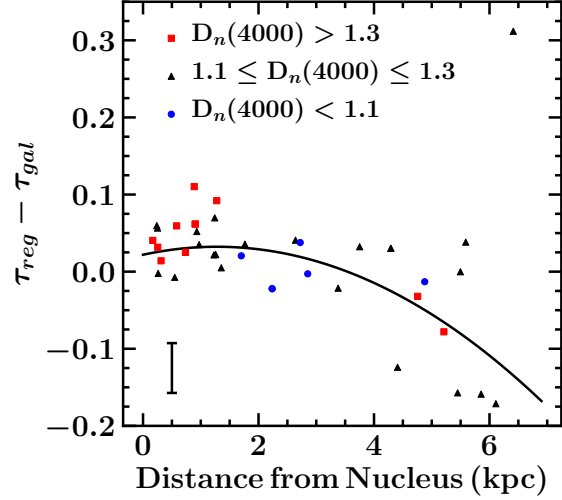


Figure 19. The difference between the τ_B^l measurements for the individual regions and that for the integrated galaxy light vs. distance from the nucleus, colour-coded by $D_n(4000)$. The second order polynomial distribution, shown by the black line, is a fit to the data. The discrepant point on the top right is also the region with the highest $\tau_B^l \approx 0.8$, and is excluded from the fit. The error bar in the lower left corner represents the characteristic uncertainty for these measurements.

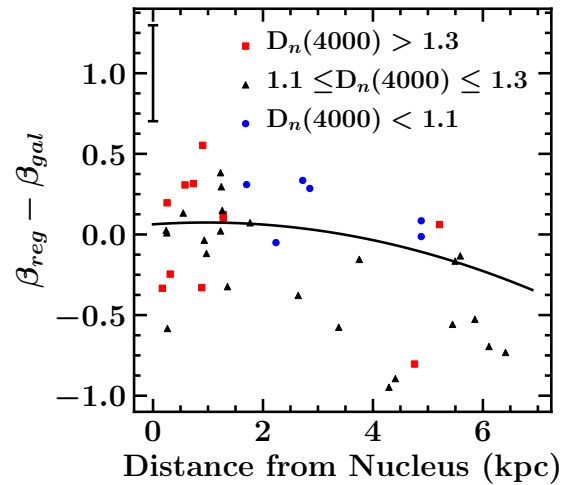


Figure 20. The difference between the measured β values for individual regions and galaxy light vs. distance from the nucleus, colour-coded by $D_n(4000)$. The error bar in the top left corner represents the characteristic uncertainty of the measurements. The second order polynomial shown in Figure 19 is translated from $\Delta\tau_B^l$ to $\Delta\beta$ using the B16 relation (black line), as the large scatter prevents us from obtaining a robust fit.

tance of ~ 6 kpc is the region with the highest $\tau_B^l \approx 0.8$, is the only such measurement in that region of parameter space, and is excluded from the fit. We colour-code by $D_n(4000)$, but do not see any systematic trends associated with that parameter.

If we translate the fit from $\Delta\tau_B^l$ to $\Delta\beta$ using the B16 relation, the data qualitatively show a correlation that agrees with the fitted relation. However, the large intrinsic scatter

undermines the utility of this diagnostic. Indeed, the average deviation of the measured vs. expected $\Delta\beta$ is 0.277. The reason for the large scatter could be attributed to a number of causes, such as the reliability of the β parameter given the SFH within the past few 100 Myr, the influence of the underlying older stellar population, the total dust content of the individual region, or the SFR seen in the observed region. To test for effects due to the underlying stellar population, we colour-code by $D_n(4000)$ in Figures 19 and 20. We see no clear correlation with $D_n(4000)$, and find this trend persists, even when excluding the regions with $D_n(4000) > 1.3$. The scatter in β is not simply due to changes in $D_n(4000)$, as evident by Figure 20.

We similarly test for the effects caused by the DIG seen in the observed region by colour-coding our relation according to $\Sigma_{H\alpha}$ in Figures 21–23. We note that the regions that with sparse star formation ($\Sigma_{H\alpha} \leq 10^{38.4} \text{ erg s}^{-1} \text{ kpc}^{-2}$) introduce significant scatter in the $\Delta\tau_B^I$ –distance relation. When these sparse regions are excluded, the resulting fit given by

$$\Delta\tau_B^I = -0.00851d^2 + 0.02082d + 0.02298. \quad (4)$$

We show this fit in Figure 22. If we translate this relation and exclude the sparse star forming regions, the $\Delta\beta$ –distance relation is well-described by the model, as shown in Figure 23. The best-fit model has an average deviation from the predicted value of 0.23, and a dispersion of $\sigma_{\text{disp}} = 0.28$. This indicates that the regions with $\Sigma_{H\alpha} < 10^{38.4} \text{ erg s}^{-1} \text{ kpc}^{-2}$ contribute to the scatter seen in the $\Delta\beta$ –distance relation. Finally, we do note a qualitative difference between those regions with high $\Sigma_{H\alpha}$ (approximately starburst-like) and those that are “star-forming”. A K-S 2-Sample test shows the two samples are distinct at the 95% confidence level. This could be indicative of the change in dust structure as a function of sSFR. However, given the small number of regions in each category, we do not attempt to further quantify this behavior.

Another strong contributor to this deviation could be the shape of the attenuation curve. Numerous papers have been written on the variation between the ratio of infrared to UV luminosity (IRX) and the slope of the UV stellar continuum (β ; e.g., Salim & Boquien 2019, for a sample of reasonably star forming galaxies). However, a much larger sample would be needed to disentangle these different possibilities.

We conclude that the deviation from the integrated measure of nebular attenuation clearly scales as a function of distance from the nucleus, while that for the stellar continuum attenuation is dependent on both distance and $\Sigma_{H\alpha}$. While the correlation between $\Delta\beta$ and distance is relatively strong for high $\Sigma_{H\alpha}$ regions, the large uncertainty, small number of data points and significant scatter prevents us from obtaining a useful fit.

7.2.2 $D_n(4000)$, Metallicity, and Other Parameters

We compared the deviation in β and τ_B^I between local and global scales to the metallicity and three different $D_n(4000)$ measurements: those from (1) the integrated galaxy light, (2) the individual star forming regions, and (3) the difference between (1) and (2). The scatter in both β and τ_B^I increases with both the metallicity and the $D_n(4000)$ index of

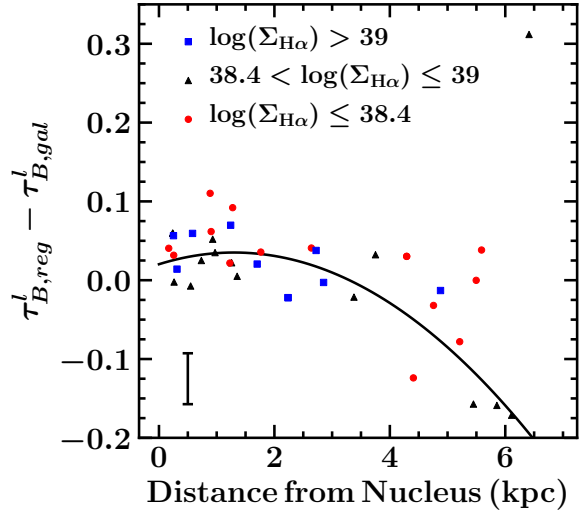


Figure 21. Same as Figure 19, except colour-coded according to $\Sigma_{H\alpha}$, which is presented in units of $\text{erg s}^{-1} \text{ kpc}^{-2}$. The regions with sparse star formation significantly contribute to the scatter seen in the relation.

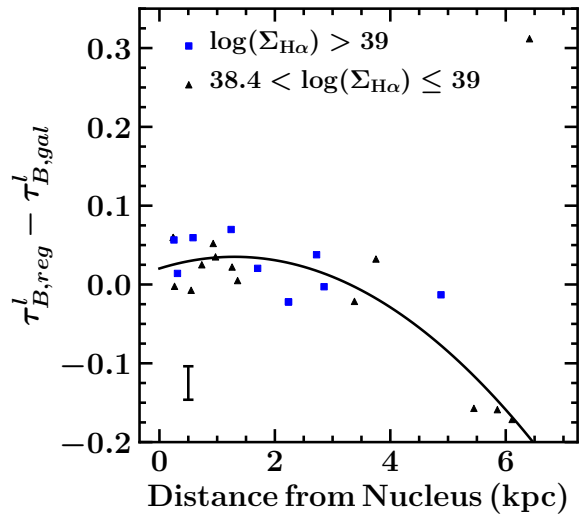


Figure 22. Same as Figure 21, but excluding “sparse” star forming regions ($\Sigma_{H\alpha} < 10^{38.4} \text{ erg s}^{-1} \text{ kpc}^{-2}$). The second order polynomial shown is from Equation (4).

the individual regions. We find a qualitative trend between $D_{\text{reg}}(4000)$ and $D_{n,\text{reg}}(4000) - D_{n,\text{gal}}(4000)$ with respect to $\beta_{\text{reg}} - \beta_{\text{gal}}$. Spearman and Kendall correlation tests both find a correlation which is significant at the 95% confidence level. However, the large dispersion makes any quantitative description of the trend difficult. Additionally, for large deviations in either direction, the assumed relation does not hold well. Therefore, while the effect of the underlying older stellar population is definitely contributing, it cannot be the only factor causing the observed scatter between local and integrated measures of attenuation based on β . In addition to the physical properties described above, we also tested for the dependence of $\Delta\beta$ and $\Delta\tau_B^I$ on $\Sigma_{H\alpha}$, and the stellar mass and SFR of the parent galaxy, but we found no significant correlations.

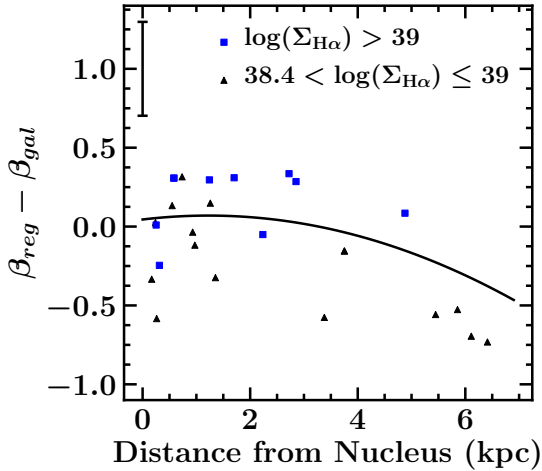


Figure 23. The difference between the measured β values for the individual regions and galaxy light vs. distance from the nucleus, colour-coded by $\Sigma_{H\alpha}$, which is presented in units of $\text{erg s}^{-1} \text{kpc}^{-2}$. The error bar in the top left corner represents the characteristic uncertainty. The second order polynomial shown in Figure 19 is translated from $\Delta\tau_B^l$ to $\Delta\beta$ using the B16 relation (black line), when the sparse star forming regions are excluded. The resulting dispersion associated with the fit is $\sigma_{\text{disp}} = 0.28$.

8 SUMMARY AND DISCUSSION

In this work, we introduced a sample of 29 nearby star forming galaxies that have both MaNGA and *Swift*/UVOT data. This sample is a subset of a larger set of galaxies which will be used for a number of other investigations including the quenching of star formation (Molina et al. in preparation). We compared the measured UV spectral slope, β , and Balmer optical depth, τ_B^l , of both the integrated galaxy light and individual kpc-sized star forming regions within the galaxies to the relation described in B16. Our goal was to test the validity of the B16 relation across the faces of galaxies and for the integrated galaxy light, as well as to study the dependence of β and τ_B^l measurements on aperture size. While the results of this paper are limited by our sample size, they also illustrate the importance of comparing integrated to spatially-resolved measures of attenuation within a single galaxy.

A region's age as probed by $D_n(4000)$, its SFR, metallicity, parent galaxy's mass and SFR all contribute to the observed scatter in the β - τ_B^l relation. Specifically, $D_n(4000)$ appears to be a useful indicator of the observed slope of the β - τ_B^l relation, with older stellar populations having steeper slopes and higher intercepts. This effect cannot be attributed to the dilution of β by the older stars alone, as shown in Figure 9. We agree with B16 that taking stellar age into account via $D_n(4000)$ is important when adopting an attenuation curve. However, we find large systematic offsets for star forming regions outside of the range $1.1 \leq D_n(4000) \leq 1.3$, which was used to define the B16 β - τ_B^l relation. We caution against using the B16 attenuation law in areas with more extreme $D_n(4000)$ values.

The SFR of an individual region is a key factor in our study, as the interpretation of β relies on the assumption that the UV light is dominated by the light of young

stars. Regions with lower SFRs could be dominated by DIG, and represent a very different physical environment than those dominated by star formation. A demarcation at $\Sigma_{H\alpha} > 10^{38} \text{ erg s}^{-1} \text{kpc}^{-2}$ in conjunction with $\text{EW}(H\alpha) > 15\text{\AA}$ appears sufficient for discriminating between these two regimes.

The relation between metallicity and β or τ_B^l described in B16 holds for individual kpc-sized regions; however there is significant scatter at high values of τ_B^l . To agree with the B16 β vs. metallicity relation, one must use all star forming regions regardless of their measured $D_n(4000)$, as per the method used by B16 in their original derivation. However, their fitted β - τ_B^l relation is limited to a specific range in $D_n(4000)$. Therefore, caution must be used when utilizing the β -metallicity and β - τ_B^l relations concurrently.

Similarly, the mass of the parent galaxy affects the observed slope of not only the integrated light, similar to that seen in Salim et al. (2018, and references therein), but also that of the kpc-sized regions. For both the integrated galaxy light and the individual star forming regions, lower-mass galaxies tend to have a steeper UV attenuation law than that of the higher-mass galaxies. This behavior could be attributed to both dust type and dust content as well as properties of the observed stars and gas within the region. The dust responsible for the attenuation can be different in low-mass galaxies, as total dust content is lower (Moustakas et al. 2006; Zhu et al. 2009), and the composition and geometry of the gas can also differ (Calzetti 2001; Kong et al. 2004; Gordon et al. 2004). The former is related to the mass of the galaxy, while the latter is strongly tied to the SFR, stellar population, and the physical structure of the star forming regions. As these regions are independent from one another, their dust compositions and geometries, mean stellar age, metallicity and structure can be unique. However, the global dust composition and metallicity will be set by the environment, i.e., the host galaxy. Therefore the similar global conditions for low-mass galaxies may be the driver of the change in the observed UV attenuation law.

Finally, the measured τ_B^l and β from the integrated galaxy light and kpc-sized star forming regions show drastically different behaviors. β displays significant variation not present in τ_B^l , even when accounting for the change in total attenuation between the two bands. The small change in τ_B^l with distance from the nucleus is well characterized by a second order polynomial fit. Conversely, the scatter in β shows marginal dependence on both position in the galaxy and deviation in $D_n(4000)$ from that of the integrated galaxy light. We therefore cannot statistically identify any one parameter as the main cause of the deviation in β .

Physically, the difference in the variation in β and τ_B^l could be explained by either sightline dependence, the dilution of β , or a combination of the two effects. The nebular emission is not as strongly affected by the observed line of sight because of the large extent of the ionized gas and the fact that it involves isotropic radiation. Conversely the star forming regions are confined spatially within galaxies, forcing the UV attenuation of the continua of the young stars to be much more dependent on the small-scale dust distribution (i.e., granularity) within and between star-forming regions. Therefore, β will have a much stronger dependence on both the sightline and aperture used than τ_B^l . Additionally, the increased contribution from the older stellar populations in

the larger aperture, as well as low area-specific SFRs in the individual regions, could be a contributing factor to the scatter in β for some of the less vigorous star forming galaxies. All of these effects could combine to create the small variation in τ_B^I and the large variation in β seen in Figures 19–23.

We conclude that agreement with the B16 β – τ_B^I model for kpc-sized star forming regions is limited to the specific parameter range of $1.1 \leq D_n(4000) \leq 1.3$, $\Sigma_{H\alpha} > 10^{38} \text{ erg s}^{-1} \text{ kpc}^{-2}$ and $\text{EW}(H\alpha) > 15 \text{ \AA}$. While the overall qualitative trend between UV stellar continuum and optical nebular attenuation holds, adopting the B16 relation for specific objects will result in large uncertainties due to variation in physical properties, such as the SFR and the age of the underlying stellar population. The integrated light also qualitatively follows the B16 relation but with significant scatter. Finally, aperture size can greatly affect the measured β and thus the adopted value of total attenuation. Therefore, while the B16 relation provides an accurate qualitative description for both the integrated galaxy light and kpc-sized star forming regions, the large scatter due to the dependence on a variety of physical parameters makes this a multi-parameter problem that requires a more comprehensive dataset to address properly.

ACKNOWLEDGEMENTS

We thank the anonymous referee for insightful comments that helped us improve this paper. We thank Lea Hagen and Michael Siegel for their help with some of the technical aspects of this work. This work was supported by funding from the Alfred P. Sloan Foundation’s Minority Ph.D. (MPHD) Program, awarded to MM in 2014–15. This research has made use of data and/or software provided by the High Energy Astrophysics Science Archive Research Center (HEASARC), which is a service of the Astrophysics Science Division at NASA/GSFC and the High Energy Astrophysics Division of the Smithsonian Astrophysical Observatory. This research made use of Astropy, a community-developed core Python package for Astronomy (Astropy Collaboration, 2018). This research has made use of the NASA/IPAC Extragalactic Database (NED), which is operated by the Jet Propulsion Laboratory, California Institute of Technology, under contract with the National Aeronautics and Space Administration. The Institute for Gravitation and the Cosmos is supported by the Eberly College of Science and the Office of the Senior Vice President for Research at the Pennsylvania State University. Funding for the Sloan Digital Sky Survey IV has been provided by the Alfred P. Sloan Foundation, the U.S. Department of Energy Office of Science, and the Participating Institutions. SDSS-IV acknowledges support and resources from the Center for High-Performance Computing at the University of Utah. The SDSS web site is www.sdss.org.

SDSS-IV is managed by the Astrophysical Research Consortium for the Participating Institutions of the SDSS Collaboration including the Brazilian Participation Group, the Carnegie Institution for Science, Carnegie Mellon University, the Chilean Participation Group, the French Participation Group, Harvard-Smithsonian Center for Astrophysics, Instituto de Astrofísica de Canarias, The Johns Hopkins University, Kavli Institute for the Physics and

Mathematics of the Universe (IPMU) / University of Tokyo, the Korean Participation Group, Lawrence Berkeley National Laboratory, Leibniz Institut für Astrophysik Potsdam (AIP), Max-Planck-Institut für Astronomie (MPIA Heidelberg), Max-Planck-Institut für Astrophysik (MPA Garching), Max-Planck-Institut für Extraterrestrische Physik (MPE), National Astronomical Observatories of China, New Mexico State University, New York University, University of Notre Dame, Observatório Nacional / MCTI, The Ohio State University, Pennsylvania State University, Shanghai Astronomical Observatory, United Kingdom Participation Group, Universidad Nacional Autónoma de México, University of Arizona, University of Colorado Boulder, University of Oxford, University of Portsmouth, University of Utah, University of Virginia, University of Washington, University of Wisconsin, Vanderbilt University, and Yale University.

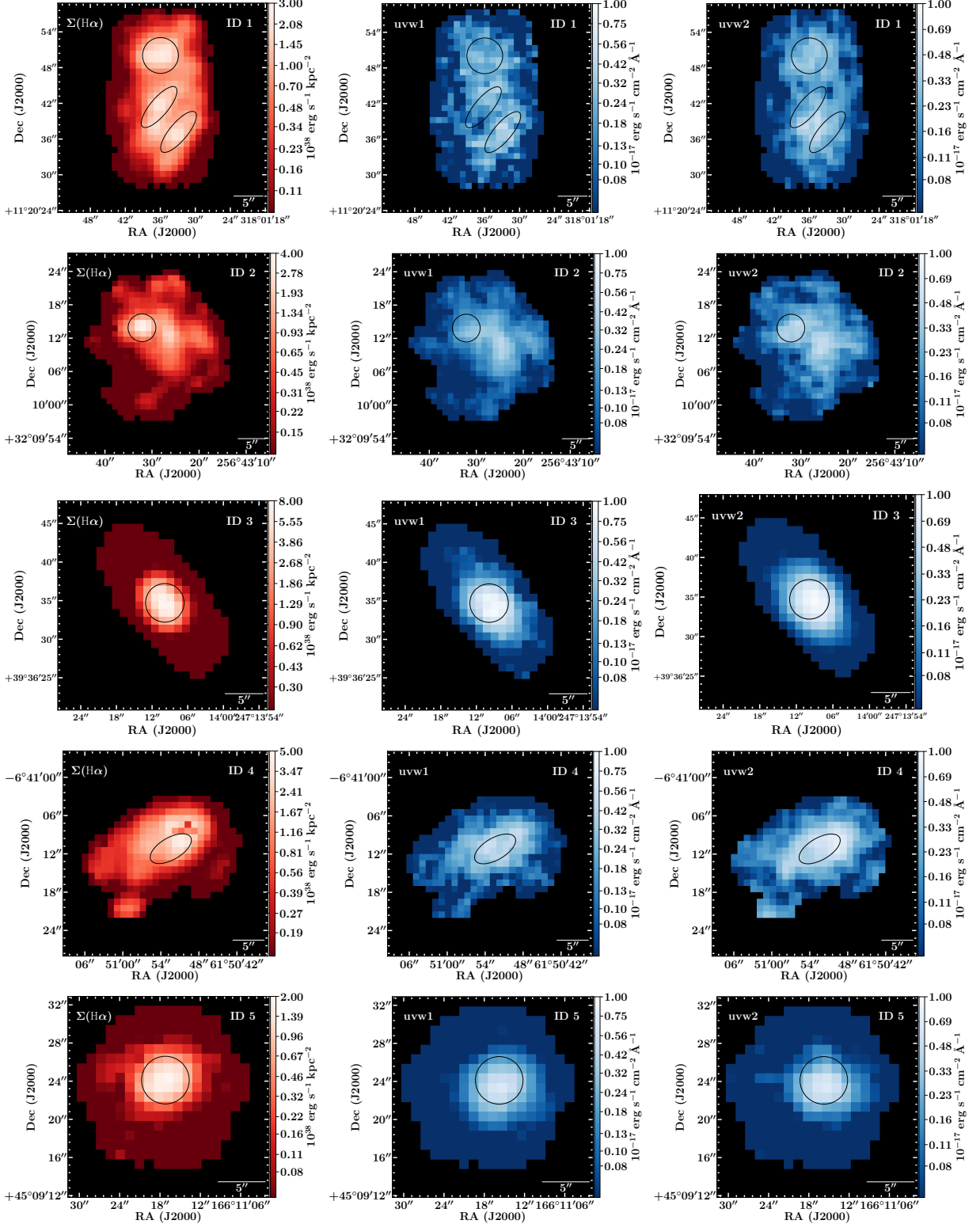
REFERENCES

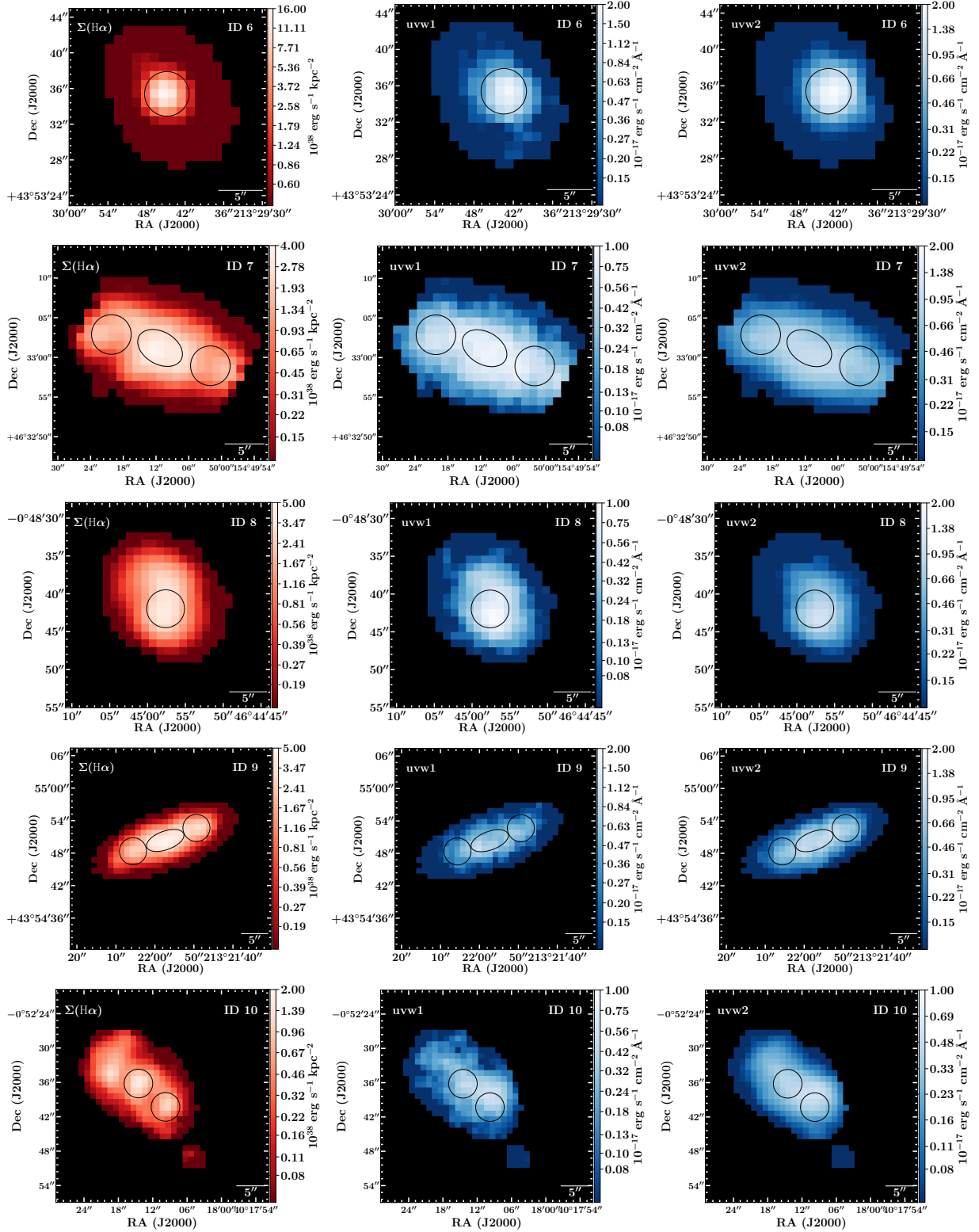
- Aguado D. S., et al., 2019, *ApJS*, 240, 23
- Bacon R., et al., 2001, *MNRAS*, 326, 23
- Baldwin J. A., Phillips M. M., Terlevich R., 1981, *PASP*, 93, 5
- Balogh M. L., Morris S. L., Yee H. K. C., Carlberg R. G., Ellingson E., 1999, *ApJ*, 527, 54
- Battisti A. J., Calzetti D., Chary R.-R., 2016, *ApJ*, 818, 13
- Battisti A. J., Calzetti D., Chary R. R., 2017, *ApJ*, 851, 90
- Belfiore F., et al., 2019, *AJ*, 158, 160
- Bershady M. A., Verheijen M. A. W., Swaters R. A., Andersen D. R., Westfall K. B., Martinsson T., 2010, *ApJ*, 716, 198
- Bertin E., Arnouts S., 1996, *A&AS*, 117, 393
- Blanton M. R., Kazin E., Muna D., Weaver B. A., Price-Whelan A., 2011, *AJ*, 142, 31
- Blanton M. R., et al., 2017, *AJ*, 154, 28
- Boissier S., et al., 2007, *ApJS*, 173, 524
- Bolton A. S., et al., 2012, *AJ*, 144, 144
- Boquien M., et al., 2009, *ApJ*, 706, 553
- Boquien M., et al., 2012, *A&A*, 539, A145
- Breeveld A. A., et al., 2010, *MNRAS*, 406, 1687
- Brinchmann J., Charlot S., White S. D. M., Tremonti C., Kauffmann G., Heckman T., Brinkmann J., 2004, *MNRAS*, 351, 1151
- Bruzual G., Charlot S., 2003, *MNRAS*, 344, 1000
- Buat V., Boselli A., Gavazzi G., Bonfanti C., 2002, *A&A*, 383, 801
- Buat V., et al., 2005, *ApJ*, 619, L51
- Bundy K., et al., 2015, *ApJ*, 798, 7
- Calzetti D., 2001, *PASP*, 113, 1449
- Calzetti D., 2013, *Star Formation Rate Indicators*. p. 419
- Calzetti D., Kinney A. L., Storchi-Bergmann T., 1994, *ApJ*, 429, 582
- Calzetti D., Armus L., Bohlin R. C., Kinney A. L., Koornneef J., Storchi-Bergmann T., 2000, *ApJ*, 533, 682
- Calzetti D., et al., 2005, *ApJ*, 633, 871
- Calzetti D., et al., 2015, *ApJ*, 811, 75
- Cappellari M., Copin Y., 2003, *MNRAS*, 342, 345
- Cappellari M., Emsellem E., 2004, *PASP*, 116, 138
- Cappellari M., et al., 2011, *MNRAS*, 413, 813
- Cardelli J. A., Clayton G. C., Mathis J. S., 1989, *ApJ*, 345, 245
- Charlot S., Fall S. M., 2000, *ApJ*, 539, 718
- Croom S. M., et al., 2012, *MNRAS*, 421, 872
- Dale D. A., et al., 2009, *ApJ*, 703, 517
- Decleir M., et al., 2019, *MNRAS*, 486, 743
- Drory N., et al., 2015, *AJ*, 149, 77
- Evans P. A., et al., 2013, *The Astrophysical Journal Supplement Series*, 210, 8

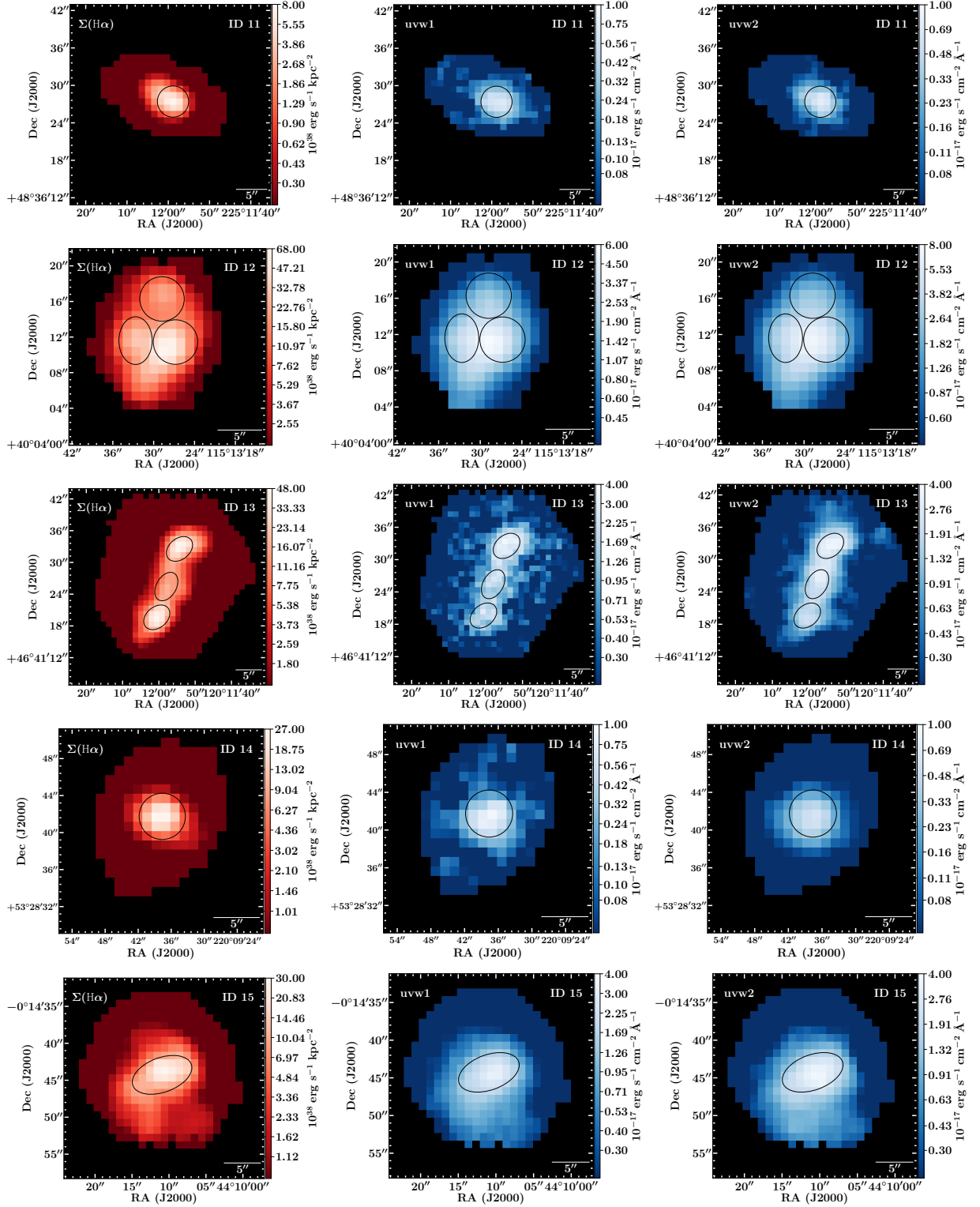
- Fitzpatrick E. L., 1999, *PASP*, 111, 63
- Giovanelli R., Haynes M. P., Salzer J. J., Wegner G., da Costa L. N., Freudling W., 1994, *AJ*, 107, 2036
- Gordon K. D., Clayton G. C., Misselt K. A., Landolt A. U., Wolff M. J., 2003, *ApJ*, 594, 279
- Gordon K. D., et al., 2004, *ApJS*, 154, 215
- Gunn J. E., et al., 2006, *AJ*, 131, 2332
- Kauffmann G., et al., 2003, *MNRAS*, 346, 1055
- Kendall M. G., 1938, *Biometrika*, 30, 81
- Kennicutt Jr. R. C., 1998, *ARA&A*, 36, 189
- Kennicutt R. C., Evans N. J., 2012, *ARA&A*, 50, 531
- Kewley L. J., Ellison S. L., 2008, *ApJ*, 681, 1183
- Kewley L. J., Dopita M. A., Sutherland R. S., Heisler C. A., Trevena J., 2001, *ApJ*, 556, 121
- Kewley L. J., Groves B., Kauffmann G., Heckman T., 2006, *MNRAS*, 372, 961
- Kong X., Charlot S., Brinchmann J., Fall S. M., 2004, *MNRAS*, 349, 769
- Law D. R., et al., 2016, *AJ*, 152, 83
- Leitherer C., et al., 1999, *ApJS*, 123, 3
- Martin D. C., et al., 2005, *ApJ*, 619, L1
- Meurer G. R., Heckman T. M., Calzetti D., 1999, *ApJ*, 521, 64
- Moustakas J., Kennicutt Jr. R. C., Tremonti C. A., 2006, *ApJ*, 642, 775
- O'Donnell J. E., 1994, *ApJ*, 422, 158
- Oey M. S., et al., 2007, *ApJ*, 661, 801
- Osterbrock D. E., Ferland G. J., 2006, *Astrophysics of gaseous nebulae and active galactic nuclei*
- Peletier R. F., Valentijn E. A., Moorwood A. F. M., Freudling W., Knapen J. H., Beckman J. E., 1995, *A&A*, 300, L1
- Petrosian V., 1976, *ApJ*, 209, L1
- Pettini M., Pagel B. E. J., 2004, *MNRAS*, 348, L59
- Poole T. S., et al., 2008, *MNRAS*, 383, 627
- Roming P. W. A., et al., 2005, *Space Sci. Rev.*, 120, 95
- Salim S., Boquien M., 2019, *ApJ*, 872, 23
- Salim S., Boquien M., Lee J. C., 2018, *ApJ*, 859, 11
- Sánchez-Blázquez P., et al., 2006, *MNRAS*, 371, 703
- Sánchez S. F., et al., 2012, *A&A*, 538, A8
- Sánchez S. F., et al., 2014, *A&A*, 563, A49
- Sánchez S. F., et al., 2016, *A&A*, 594, A36
- Schlegel D. J., Finkbeiner D. P., Davis M., 1998, *ApJ*, 500, 525
- Smee S. A., et al., 2013, *AJ*, 146, 32
- Spearman C., 1904, *The American Journal of Psychology*, 15, 72
- Stephens M. A., 1974, *Journal of the American Statistical Association*, 69, 730
- Tremonti C. A., et al., 2004, *ApJ*, 613, 898
- Wake D. A., et al., 2017, *AJ*, 154, 86
- Walcher C. J., et al., 2014, *A&A*, 569, A1
- Wang E., et al., 2018, *ApJ*, 856, 137
- Westfall K. B., et al., 2019, *arXiv e-prints*, p. arXiv:1901.00856
- Wild V., Charlot S., Brinchmann J., Heckman T., Vince O., Pacifici C., Chevallard J., 2011, *MNRAS*, 417, 1760
- Xiao T., Wang T., Wang H., Zhou H., Lu H., Dong X., 2012, *MNRAS*, 421, 486
- Yan R., et al., 2016, *AJ*, 152, 197
- Zhang K., et al., 2017, *MNRAS*, 466, 3217
- Zhu G., Moustakas J., Blanton M. R., 2009, *ApJ*, 701, 86

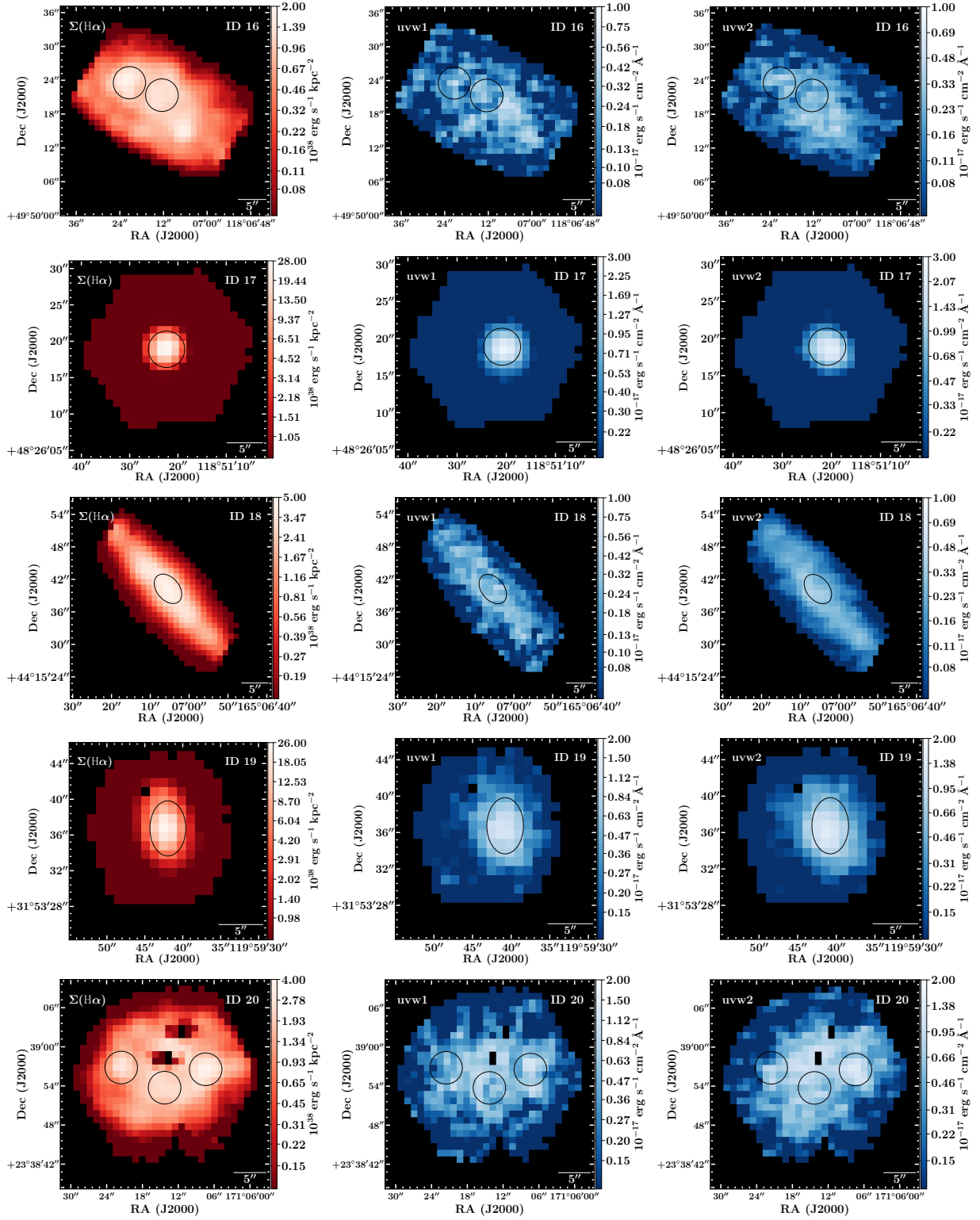
APPENDIX A: IDENTIFIED STAR FORMING REGIONS

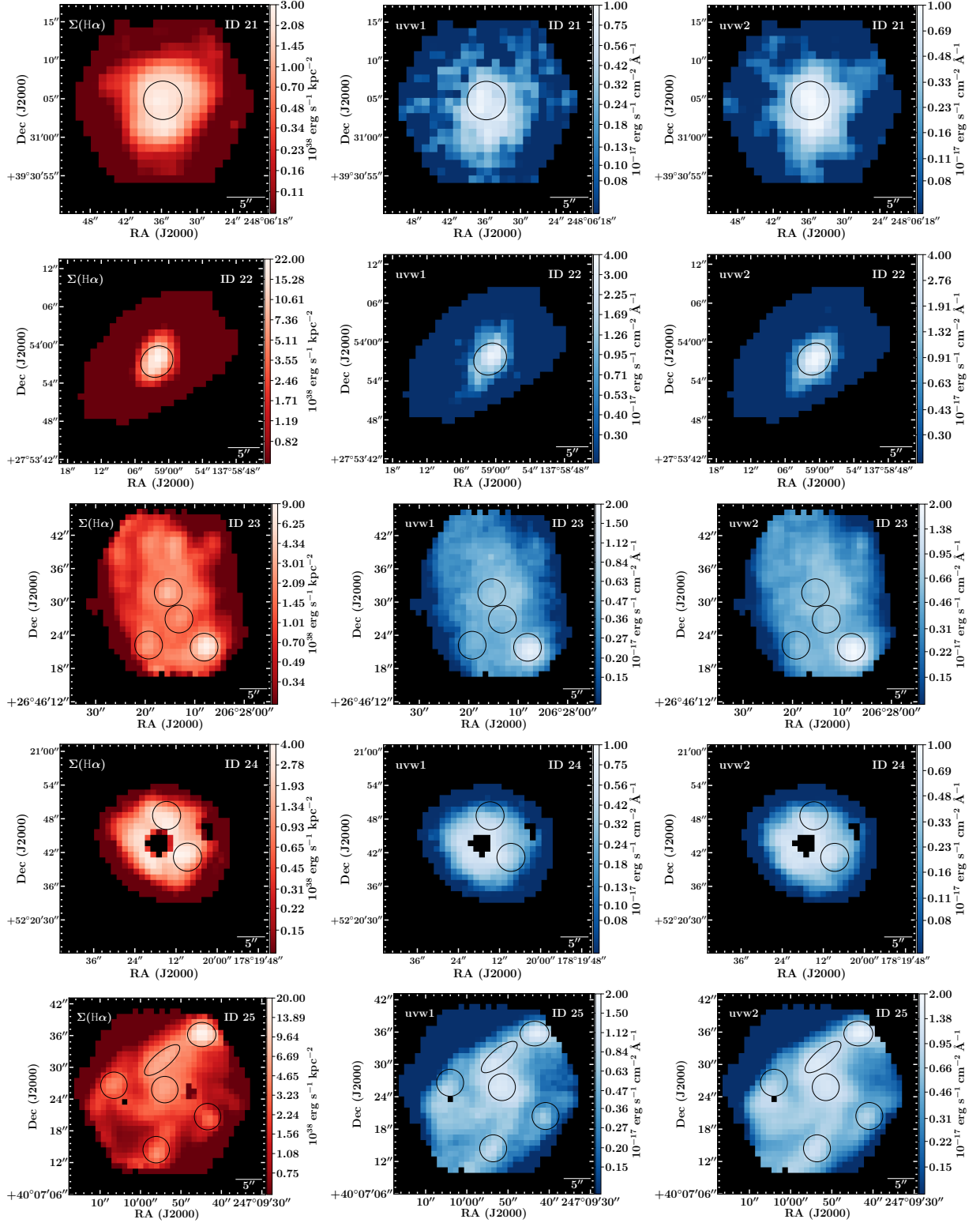
In this appendix, we present $\Sigma_{\text{H}\alpha}$, uvw2 and uvw1 images of the 29 galaxies with the individual regions indicated by the black apertures. The objects are labelled by the object IDs listed in Table 2. We used a conservative approach to define star forming regions; each region must: (1) have a brightness peak with the observed $\Sigma_{\text{H}\alpha} \geq 10^{38} \text{ erg s}^{-1} \text{ kpc}^{-2}$ and (2) appear star forming in all three BPT diagrams. Therefore, there may be bright regions in the $\Sigma_{\text{H}\alpha}$ maps that are not identified as a star forming region. Finally, we also include a table with the positions, radii, b/a and θ values for the regions in Table A1.











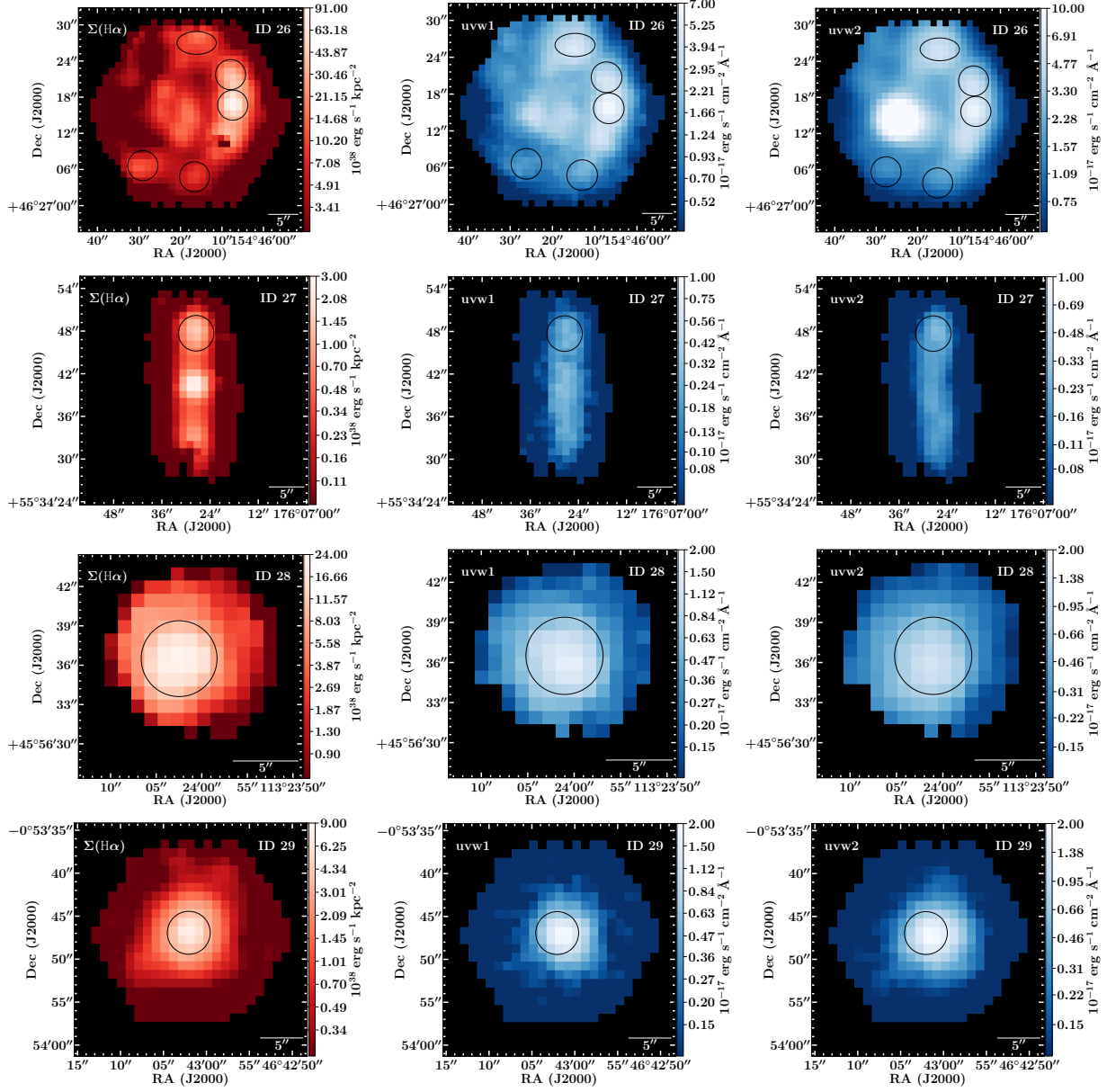


Table A1. Aperture Definitions for Star Forming Regions

Region I.D.	R.A. (deg)	Dec. (deg)	a (arcsec)	b/a	θ (deg)
1.1	318.02666	11.34723	3.01130	1	...
1.2	318.02644	11.34511	4.32769	0.34522	50
1.3	318.02580	11.34366	4.32769	0.34522	50
2.1	256.72559	32.17052	2.5	1	...
3.1	247.23607	39.60964	2.5	1	...
4.1	61.84818	-6.68616	3.59562	0.47922	150
5.1	166.18811	45.15670	2.5	1	...
6.1	213.49579	43.89317	2.5	1	...
7.1	154.83646	46.55033	3.03785	0.67213	150
7.2	154.83390	46.54971	2.5	1	...
7.3	154.83894	46.55080	2.5	1	...
8.1	46.74934	-0.81166	2.5	1	...
9.1	213.36593	43.91398	3.62550	0.47253	20
9.2	213.36371	43.91462	2.5	1	...
9.3	213.36823	43.91343	2.5	1	...
10.1	40.30403	-0.87672	2.5	1	...
10.2	40.30271	-0.87786	2.5	1	...
11.1	225.19968	48.60762	2.5	1	...
12.1	115.22574	40.06989	2.68115	0.69767	90
12.2	115.22466	40.07119	2.5	1	...
12.3	115.22411	40.06984	2.5	1	...
13.1	120.19842	46.69237	2.77694	0.71108	40
13.2	120.19943	46.69040	2.91361	0.64391	60
13.3	120.20016	46.68878	2.76588	0.71108	40
14.1	220.16045	53.47826	2.5	1	...
15.1	44.16970	-0.24563	4.20687	0.55542	20
16.1	118.12012	49.83926	2.89310	1	...
16.2	118.12260	49.83988	2.86452	1	...
17.1	118.85621	48.43858	2.5	1	...
18.1	165.11818	44.26118	3.08765	0.67097	130
19.1	119.99499	31.89354	3.08765	0.65161	90
20.1	171.10206	23.64904	2.5	1	...
20.2	171.10397	23.64826	2.5	1	...
20.3	171.10599	23.64916	2.5	1	...
21.1	248.10994	39.51800	2.5	1	...
22.1	137.98392	27.89927	2.65936	0.87641	40
23.1	206.47093	26.77547	2.5	1	...
23.2	206.47033	26.77414	2.5	1	...
23.3	206.47203	26.77284	2.5	1	...
23.4	206.46895	26.77273	2.5	1	...
24.1	178.33743	52.34683	2.5	1	...
24.2	178.33574	52.34477	2.5	1	...
25.1	247.16206	40.12241	2.5	1	...
25.2	247.16246	40.12662	2.69824	0.84901	0
25.3	247.16518	40.12538	4.17331	0.35561	40
25.4	247.16500	40.12383	2.5	1	...
25.5	247.16849	40.12406	2.5	1	...
25.6	247.16559	40.12068	2.5	1	...
26.1	154.77128	46.45133	2.5	1	...
26.2	154.76872	46.45463	2.5	1	...
26.3	154.76887	46.45604	2.5	1	...
26.4	154.77140	46.45750	3.26693	0.57927	0
26.5	154.77514	46.45156	2.5	1	...
27.1	176.12429	55.57992	2.5	1	...
28.1	113.40069	45.94347	2.89125	1	...
29.1	46.71724	-0.89637	2.5	1	...